

Article

Optimization of the Design of Underground Hydrogen Storage in Salt Caverns in Southern Ontario, Canada

Jingyu Huang and Shunde Yin *

Department of Civil and Environmental Engineering, University of Waterloo, Waterloo, ON N2L 3G1, Canada; j583huang@uwaterloo.ca

* Correspondence: shunde.yin@uwaterloo.ca

Abstract: With the issue of energy shortages becoming increasingly serious, the need to shift to sustainable and clean energy sources has become urgent. However, due to the intermittent nature of most renewable energy sources, developing underground hydrogen storage (UHS) systems as backup energy solutions offers a promising solution. The thick and regionally extensive salt deposits in Unit B of Southern Ontario, Canada, have demonstrated significant potential for supporting such storage systems. Based on the stratigraphy statistics of unit B, this study investigates the feasibility and stability of underground hydrogen storage (UHS) in salt caverns, focusing on the effects of cavern shape, geometric parameters, and operating pressures. Three cavern shapes—cylindrical, cone-shaped, and ellipsoid-shaped—were analyzed using numerical simulations. Results indicate that cylindrical caverns with a diameter-to-height ratio of 1.5 provide the best balance between storage capacity and structural stability, while ellipsoid-shaped caverns offer reduced stress concentration but have less storage space, posing practical challenges during leaching. The results also indicate that the optimal pressure range for maintaining stability and minimizing leakage lies between 0.4 and 0.7 times the vertical in situ stress. Higher pressures increase storage capacity but lead to greater stress, displacements, and potential leakage risks, while lower pressure leads to internal extrusion tendency for cavern walls. Additionally, hydrogen leakage rate drops with the maximum working pressure, yet total leakage mass keeps a growing trend.



Academic Editors: Juan M. Menendez Aguado, Vasyi Lozynskyi, Oscar Jaime Restrepo Baena and Juan C. Lucena

Received: 14 December 2024

Revised: 13 January 2025

Accepted: 17 January 2025

Published: 22 January 2025

Citation: Huang, J.; Yin, S.Optimization of the Design of Underground Hydrogen Storage in Salt Caverns in Southern Ontario, Canada. *Mining* **2025**, *5*, 9. <https://doi.org/10.3390/mining5010009>

Copyright: © 2025 by the authors. Licensee MDPI, Basel, Switzerland. This article is an open access article distributed under the terms and conditions of the Creative Commons Attribution (CC BY) license (<https://creativecommons.org/licenses/by/4.0/>).

Keywords: renewable energy; energy storage; underground hydrogen storage; salt caverns; in situ stress; optimal design

1. Introduction

Nowadays, with the world's population projected to reach 8.7 billion by 2035, energy shortages are becoming critical, potentially leaving 1.6 billion people in shortage of energy [1]. Only relying on traditional energy sources will no longer meet the existing situation as traditional energy sources like fossil fuels, which fulfill almost 85% of the cumulative energy needs, are finite and account for 56.6% of GHG emissions (CO₂ equivalent) [2]. To address energy shortages and GHG emissions, the best way is undoubtedly shifting energy consumption from fossil-based fuels to clean and renewable energy, including but not limited to wind, solar, and hydropower [3]. Though promising, most renewable energy sources used are all inherently intermittent and depend on seasonal and weather conditions, posing obstacles to the construction of a stable energy supply system. For example, by 2024, China's wind and solar power capacities had grown to about 510 million kilowatts and 840 million kilowatts, respectively [4], yet curtailment was 57 billion kWh and 14.2 billion

kWh in 2017 due to the innate intermittency, random fluctuations, and poor dispatch ability of solar and wind energy [5], and such curtailment remains unsolved to this day [6]. To address these challenges, building complementary power systems is crucial, as they could be aligned with random fluctuations of these power systems, storing excessive energy output at its peak and releasing energy when needed.

Two main factors should be considered when designing such energy storage systems. The very first thing is the choice of energy storage form. Energy storage can be divided into six categories based on the forms: thermal energy storage, mechanical energy storage, chemical energy storage, electrochemical energy storage, electrical energy storage, and other types of energy storage. Considering the frequent cycles of extraction and storage balancing the fluctuation, chemical energy storage stands out for its stability and flexibility [7]. Among all energy storage chemicals, hydrogen (H₂), with a high specific energy capacity of 120 MJ/kg and a clean combustion product, as well as relatively inert chemical properties, shows great potential. It can replace almost 60% of the natural gas used for non-industrial activities [8].

The other crucial factor is the storage facility. H₂ has a low density of 0.089 kg/m³ under standard conditions, which is about 8 times less dense than CH₄ and 22 times less dense than CO₂ [9]. Consequently, large-scale volume and high pressure will be indispensable. In addition, to effectively balance the demand and supply during peak periods, H₂ is required to be stored on the scale of GWhr to TWhr, outreaching the capacity limit of surface storage facilities [10]. Moreover, its small molecular size poses challenges on sealing conditions.

Considering these factors, underground hydrogen storage could be the potential solution, due to its advantages over surface storage facilities: (1) keeping gas stored away from potential threats associated with fire and human activities; (2) having much vaster space, providing bigger capacity for storage and helping utilize limited space efficiently; (3) economical; (4) easily accessible; (5) providing a better-sealed and stable storage condition, as hydrogen does not typically react with rocks [11].

Conventional underground gas storage media include aquifers, depleted gas fields, and salt caverns. Aquifers, though bearing vast storage space and easy access, must have suitable reservoir properties and sealing quality to prevent gas migration and leakage. Depleted gas fields provide large gas storage potential, owing to their innate stable infrastructure with proven integrity, as they have previously trapped gas and oil migrated from the underlying source rocks for thousands of years [12]. However, residual gas can mix with the stored gas, compromising purity. In addition, gas trapped in the pore throats during extraction causes a relatively low recovery rate. Salt caverns are the most desirable medium for underground hydrogen storage. Geological assessments of salt caverns are widely conducted worldwide. In Epe, North Rhine–Westphalia, Germany, approximately 2.7 billion cubic meters of natural gas was stored in salt caverns [13]. In southeastern Alberta near Medicine Hat, Canada, around 4.4 billion cubic meters of natural gas was stored underground in salt caverns, enough to support Alberta's gas network and broader Western Canadian energy markets. The surrounding salt rock acts as a virtually impermeable seal, resulting in a leakage rate of less than 1% [14]. Furthermore, without the disturbance of other substances remaining, the gas stored in the salt caverns can reach up to 95% purity without biological or chemical reactions [15].

So far, significant progress has been made in exploring underground hydrogen storage within salt caverns. Four projects have been successfully launched in the United States (three locations) and the United Kingdom (one location) [14]. In addition, many countries have identified suitable sites through extensive geological assessments, showing a promising outlook. For example, Poza de la Sal diapir in Spain has been identified as a potential

UHS spot with an expected capacity of 23 GWh [16]. Canada is also a front-runner in this area. Bearing abundant halite resources, the Canadian government has committed significant resources to developing underground hydrogen storage. Abundant halite deposits are found in Alberta, Ontario, Saskatchewan, Manitoba, New Brunswick, and Nova Scotia. Several indispensable factors needed to be considered for UHS construction, specifically, the high purity of the halite (little to no shale/carbonate interbeds, etc.), existing mining operation conditions, locations, and the form and thickness [17], yet many sites show great potential for future UHS construction, particularly in the Western Canada Sedimentary Basin (WCSB) and in southern Ontario. These areas exhibit a relatively low risk for a catastrophic seismic or volcanic event and contain a plethora of bedded halite [18]. It is estimated that the underground storage volume of salt caverns in Ontario alone could be around 9.10 million cubic meters, equal to around 557.80 million cubic meters of working gas at standard conditions [19].

Though geological investigation of future salt caverns for UHS suggests a promising outlook, research in this field is still preliminary. Abundant studies have focused on this topic and offer strong feasibility worldwide, but most of them still remain at the prospective stage and lack down-to-earth design and simulation [20,21], and few studies on UHS salt cavern design in Ontario have been conducted. Extensive preparations are needed before designing a UHS system, among which the most fundamental one is designing the cavern shape based on stratigraphic characteristics. Salt caverns are typically constructed through leaching owing to the water-soluble property of salt. Two basic leaching methods are used: direct and indirect leaching. In direct leaching, freshwater is pumped through an inner string to the cavern bottom, where it dissolves salt and rises to the top as brine through an outer casing, typically creating a cylindrical cavern. For the indirect or reverse leaching method, on the other hand, freshwater enters through the outer casing on the top, dissolves salt at the bottom, and exits through the inner string, often resulting in a cavern with an enlarged top [22]. In addition, by adjusting the flow rate and injection point, an elliptical-shaped salt cavern can also be obtained. Regardless of the method used, a layer of insoluble sediment will always accumulate at the bottom of the cavern. A schematic depicting both methods is shown in Figure 1. Most studies assume the cavern to be cylindrical when estimating the potential UHS capacity; however, it is still of great importance to design the proper cavern shape with simulations.

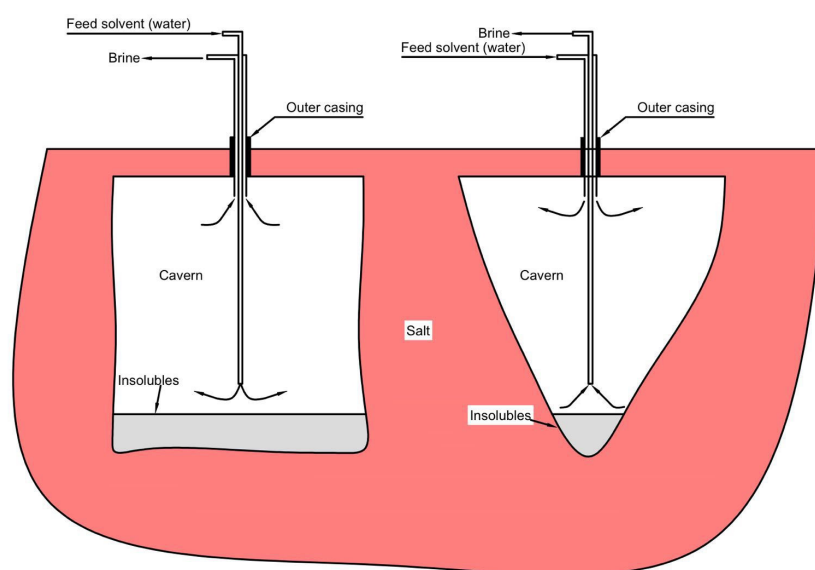


Figure 1. Salt cavern schematic showing different dissolution setups. (left) direct leaching; (right) indirect leaching.

In addition to cavern shape, the geometric parameters are also crucial when designing a salt cavern for UHS. In bedded salt deposits, the minimum height-to-diameter ratio should be 0.5 to maintain geomechanical stability. The minimum thickness of the hanging wall is suggested to be 75% of the cavern diameter, while the foot wall is advised to be 20% of the cavern diameter [15]. Some studies also recommend that the hanging wall of the salt caverns should be no less than 20 m for thin salt layers and a minimum foot wall thickness of 10 m [23,24]. Most current research in Canada on hydrogen storage in salt caverns remains preliminary. Storage volume estimations in most studies are based on the cylinder-shaped cavern with a height twice its radius [25], applying the approximate shape factor of 0.7 for calculations [24]. However, few numerical simulations have been conducted on this topic. Given the uncertainty of the cavern shape and parameters, conducting stability simulations is essential before moving forward with field construction.

Preliminary stability analysis of salt caverns is not sufficient when considering the operating pressures during injection and withdrawal cycles, especially with Ontario's fluctuating energy supply. Both injection and withdrawal will change the working gas pressure posed on the cavern walls. Inappropriate working pressure will lead to roof collapse, pillar damage, and pipe column damage. At lower working pressure, deviatoric stress within the surrounding rock increases, making it more susceptible to instability and failure. Conversely, excessively high pressure may cause plastic deformation or even fractures in the salt rock [26]. Most studies recommend maintaining working pressures between 30% and 80% of the vertical in situ stress on the cavern roof [15], but geological features remain a key factor, and detailed simulations are essential. Furthermore, as the salt cavern undergoes periodic loading and unloading during cycles, continuous deformation occurs in the salt rock due to its creep behavior. Improper operational pressure can exacerbate this deformation, potentially leading to leakage or structural failure over time [27]. Another important factor that needs to be considered is the leakage risks. Though salt rock has been proven to be perfectly sealed for hydrogen storage, interlayers in the bedded salt deposit can act as potential leakage paths due to their higher permeability. In addition, the working pressure of the stored gas will also affect such leaking behavior, as the stress field difference between the cavern and the hosting strata is the primary driving force for hydrogen migration. Therefore, simulations are required to determine the optimal operating pressure range for safe and efficient injection–withdrawal cycles.

With growing interest in using salt caverns for underground hydrogen storage (UHS), extensive experiments and analytical simulations have been conducted worldwide. While experiments primarily focus on hydrogen flow and permeability changes in salt rock caused by stress variations and thermally induced temperature fluctuations during repetitive loading and unloading cycles [28–30], simulations are increasingly adopted for UHS system designs with distinct geological characteristics of various regions. Naderi et al. developed 1D and 3D models based on geological data from stratified salt caverns in the Carribuddy Formation, Western Australia, analyzed mechanical properties and stress distribution, and thereby determined safe operation pressure ranges of the UHS system [31]. Deng et al. performed a 2D finite element analysis of an oval-shaped cavern in Jiangsu, China, focusing on the full-cycle injection and production processes of salt cavern hydrogen storage, investigating the displacement characteristics and deformation behaviors of the surrounding rock [32]. Williams et al. focused on site selection, characterization of repository properties, determination of allowable pressure and temperature ranges, and the development of constitutive models for creep. They conducted simulations of salt caverns for UHS in the Brazilian pre-salt fields [33]. However, none of these studies have specifically addressed cavern shape design, and similar simulations and analyses remain scarce in Canada. In this paper, utilizing stratigraphic data and mechanical properties of the B unit of the Salina

Group in Southern Ontario, Canada, as a demonstration base, three-dimensional geological models were established via COMSOL 6.2 software to investigate how different shapes of salt caverns impact the UHS facility stability, and how internal pressure affects the safety of salt rock cavern hydrogen storage. Under such conditions, the hydrogen leakage rate is predicted. After gaining a preliminary design proposal, the creep development of the surrounding rock is simulated to ensure long-term stability. Through simulations, the shape and design parameters of salt caverns are optimized, leading to the long-term stability of caverns, low hydrogen leakage rate, and better storage and extraction strategies.

2. Geological Setting

Salt deposits of southwestern Ontario are found in the Salina formation of Silurian age, deposited in the Michigan Basin, located in the southwestern area of the province. Based on lithology differences, the Salina Group stratum is subdivided into different units and labeled A to G. Vertically, salt rocks are distributed across different units including F, D, B, and the lower part of the A2 unit [25]. Laterally, the depths and thicknesses of these salt beds vary. For example, unit B ranges in thickness from 145 m in the basin center to less than 15 m at the margins, with depths between 275 m and 825 m, averaging 400 m in depth and 90 m in thickness. The lower A2 unit lies between 500 m and 775 m in depth, with thicknesses up to 45 m [34]. Unit B and A2 are considered potential UHS sites, while unit F not only has the shallowest depth (ranging from 275 m to 450 m), but also contains too many impurities in the form of shale and dolostone interbeds, as well as anhydrite. Unit D, bearing an average thickness of 12 m, is inadequate for UHS cavern construction [34]. Comparing the average thickness of unit B and A2, unit B is significantly thicker, providing more potential capacity for UHS. Thus, this paper will focus on the stratigraphy of unit B. The detailed lithology and the thickness of each unit are listed in Figure 2.

Formation	Gamma	Lithology	Depth (m)	Unit	Description	
Mississippian				G unit	Fine crystalline brown dolostone, shaly dolomite, some anhydrite	
Devonian		Upper			F unit	Salt, in thick beds separated by beds of shale, shaly dolostone, grey and buff and brown crystalline dolostone; anhydrite nearly always present.
		Middle		200	F salt	
		Lower		400	E unit	Thin shale unit, argillaceous grey and buff dolostone.
Silurian		Upper			D unit	Salt, nearly pure; minor, thin dolostone and shale beds.
					C unit	Lower bed of shaly anhydrite or dolostone, grading upwards to green shale with anhydrite nodules.
				600	B unit	Salt, in thick salt beds with thin shale or dolostone interbeds. The base of the B unit is marked by an anhydrite-rich zone.
				800	B salt	
Lower				A2 carbonate	Dark to light grey-brown, laminated to thin-bedded, very fine- to fine-grained dolostone and limestone.	
			1000	A2 evaporate	Salt up to 45 meters thick; where salt is absent, the base is marked by anhydrite.	
Ordovician		Upper			A1 carbonate	Very fine- to medium-grained, tan-grey to black, variably bituminous, laminated to massive dolostone and limestone.
		Middle		1200	A1 anhydrite	Anhydrite with minor dolostone and salt.
Upper Cambrian				1400	A0 carbonate	Dark brown to black, laminated, bituminous dolostone.

Figure 2. The lithology of the thickness of each unit in Ontario [19].

Based on gamma-ray (GR) and porosity (CNL) logs from testing wells within unit B, a consistent pattern emerges across all sampling points: the logs reveal two well-defined sequence boundaries. Therefore, unit B can be subdivided into three high-frequency sequence subunits, labeled SQ1, SQ2, and SQ3.

- SQ1: The upper part of unit B, characterized by high GR and CNL values, indicating a salt–limestone layer.
- SQ2: The middle section, consisting of dark bedded salt rocks, with dramatic fluctuations in GR and CNL logs.
- SQ3: The lower section, showing relatively stable trends and low GR and CNL values, corresponding to massive salt rocks.

Unit B also overlies a several-meter-thick anhydrite layer, primarily found around Wyoming and Bridgen. Figure 3 illustrates these subunits using data from wells F006864 and T003039. Each subunit is distinguished by a different color.

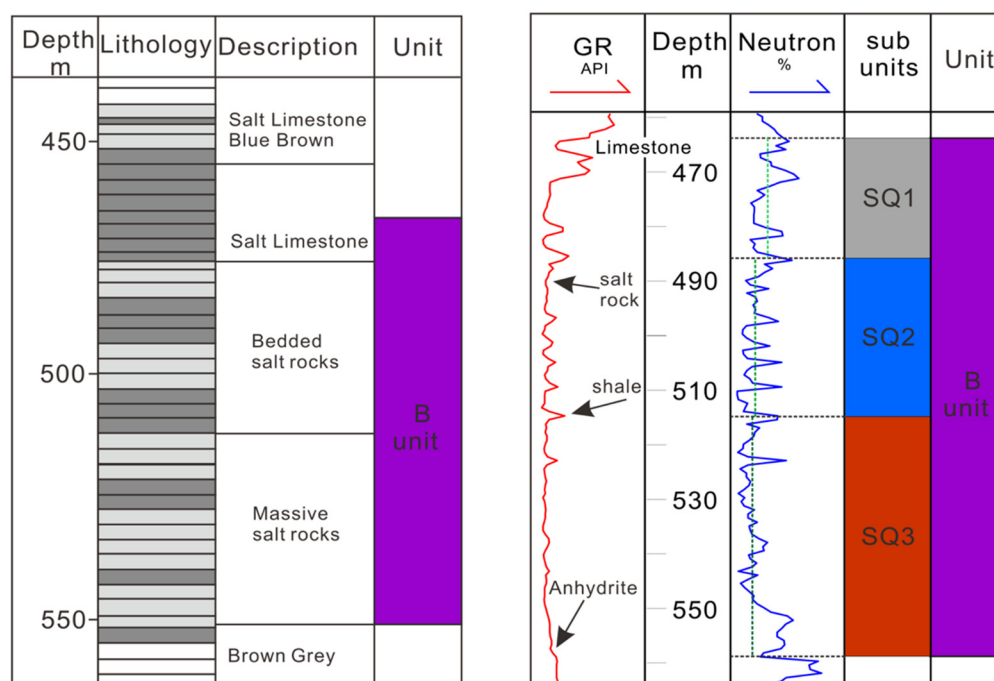


Figure 3. The core distributions and subunits of the unit B. Data taken from F006864 well (left) and T003039 well (right) [19].

The thicknesses of subunits SQ1, SQ2, and SQ3 in unit B generally range from 20 to 30 m, 25 to 35 m, and 30 to 40 m, respectively. SQ1 is not ideal for UHS because of its thin thickness and high limestone content. Figure 4 illustrates the thickness variation of these subunits in the north–south direction around Petrolia, Bridge, and Wilkesport in the central part of the Michigan Basin. In order to better represent the overall situation of unit B and better conduct UHS simulations, only subunit SQ2 and SQ3 are considered, assuming average thicknesses of 30 m and 35 m, respectively, which not only represent the average thicknesses of both subunits but also closely mimic the field conditions in the northern part of the Petrolia, as shown in Figure 4. To simplify the model, the strata are assumed to be flat, which closely matches the slight dip observed in the area. Given the randomness of shale layer distribution, as indicated by the inconsistent GR log peaks, SQ2 is modeled to include five equidistant shale layers, each 1 m thick, to represent bedded salt deposits. In contrast, the GR log of SQ3 shows relatively stable trends with low GR and CNL values, indicating a predominantly pure salt rock composition. Consequently, the entire SQ3 layer is assumed to consist of pure salt.

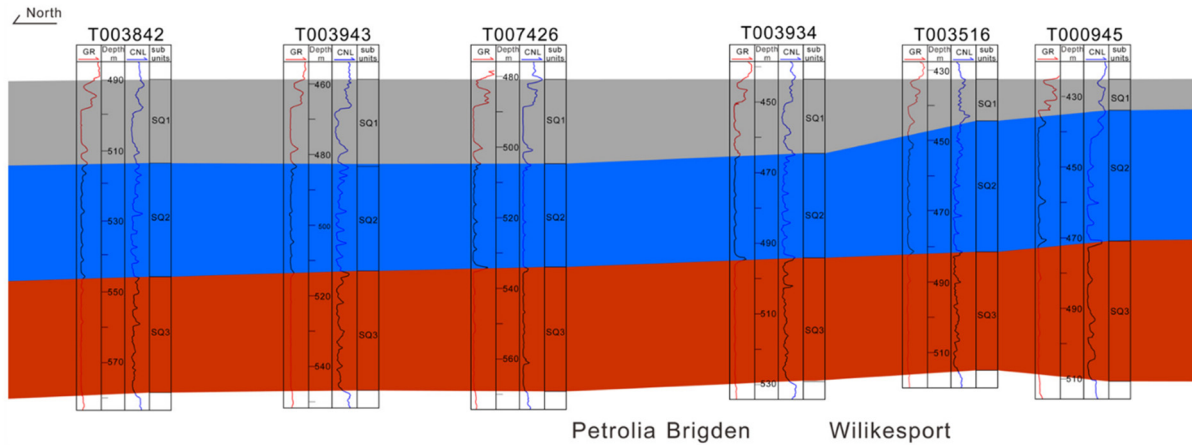


Figure 4. The thickness variation of subunits SQ1, SQ2, and SQ3 in the north–south direction [19].

The three-dimensional stratigraphic model measures 200 m × 200 m × 100 m, and consists of the following layers in top–down order:

- A 25 m thick limestone layer (SQ1) on top;
- A 30 m thick salt deposit with five evenly inserted shale layers (SQ2);
- A 35 m thick salt deposit (SQ3);
- A 3 m thick anhydrite layer embedded at the bottom;
- Another 7 m thick limestone layer beneath the anhydrite.

3. Constitutive Model

3.1. Elastoplastic Constitutive Model

In this chapter, the classic Drucker–Prager material model is adopted to simulate the elastoplastic behavior of surrounding rocks for both the initial stability after the cavern is excavated and the long-term stability during the injection–withdrawal cycles. Capturing the frictional and cohesive characteristics of materials, this model can represent initial plastic yield and shear failure of the surrounding salt rock after the cavern is excavated, representing the initial plastic deformation well, contributing to the short-term stability evaluation. This model is widely used in geotechnical engineering and petroleum engineering, especially in areas dealing with rocks with prominent plastic behaviors and focusing on short-term behaviors, like borehole drilling and cavern excavation.

Considering the compressive stress negative, the yield criterion for the Drucker–Prager model is expressed as follows [35]:

$$f(\sigma) = \sqrt{J_2} + \alpha I_1 - k = 0 \tag{1}$$

where J_2 is the second invariant of the stress deviator tensor, and I_1 is the first invariant of the stress tensor.

J_2 and I_1 are defined as follows:

$$J_2 = \frac{1}{6}[(\sigma_1 - \sigma_2)^2 + (\sigma_2 - \sigma_3)^2 + (\sigma_1 - \sigma_3)^2] \tag{2}$$

$$I_1 = \sigma_1 + \sigma_2 + \sigma_3 \tag{3}$$

and σ_1 , σ_2 , and σ_3 are the principle effective stresses. α and k are material constants connected to the material’s cohesion and friction angle. The correlations are as follows:

$$\alpha = \frac{2\sin \varphi}{\sqrt{3}(3 - \sin \varphi)} \tag{4}$$

$$k = \frac{6c \cos \varphi}{\sqrt{3}(3 - \sin \varphi)} \quad (5)$$

where φ is the internal friction angle of the rock, and c is the cohesion intercept.

3.2. Evaluation Model of Tightness

When designing an underground gas storage system, the tightness of the cavern is another crucial factor as the leakage of the gas is inevitable and will be increasingly evident over time, especially for gases with high diffusibility, low dynamic viscosity, and extremely small molecular diameter like hydrogen. Bearing these physical properties, the permeability of hydrogen is approximately six times higher than that of methane under the same pressure and surrounding conditions.

To simulate the leakage of hydrogen during the long-term injection–extraction cycles, the Darcy’s law module is applied. Darcy’s law can describe the convection of hydrogen in the porous surrounding rocks. The basic equations are as follows:

$$\frac{\partial}{\partial t}(\epsilon_p \rho) + \nabla(\rho \mathbf{u}) = Q_m \quad (6)$$

$$\mathbf{u} = -\frac{\kappa}{\mu}(\nabla p - \rho \mathbf{g}) \quad (7)$$

where ϵ_p is the porosity of the surrounding rock, ρ is the density of the hydrogen, Q_m is the mass resources, κ is the permeability of the surrounding rock, μ is the dynamic viscosity, p is the pressure, and \mathbf{u} is the permeation velocity. It is noteworthy that due to the relatively low permeability and porosity of salt rocks or shale layers compared to other rocks, the initial condition of the surrounding rocks is assumed to be completely dry, and the air inside those pores is neglected as the rock is fully compressed under high-pressure conditions underground. In addition, though neglected in this chapter, research results show that the Reynolds numbers of all strata are small enough to consider that hydrogen flow in the surrounding salt rock conforms to Darcy’s law. The equation takes gravity into consideration and assumes the hosting rock to be isotropic.

Considering the porous rock background, the equation can be written as follows:

$$\rho s_p \frac{\partial \rho}{\partial t} + \nabla(\rho \mathbf{u}) = Q_m \quad (8)$$

$$s_p = \epsilon_p \chi_f + (1 - \epsilon_p) \chi_p \quad (9)$$

where χ_f is the compressibility of hydrogen, and χ_p is the compressibility of hosting rock.

3.3. Creep Constitutive Model

In this study, Norton creep equation is adopted to simulate the creep behavior of salt rocks. The creep equation is expressed as follows [26]:

$$\dot{\epsilon}(t) = Aq^n \quad (10)$$

where A and q are rock creep variables, and q is a variable connected to stress. The correlation between q and stress is expressed as follows:

$$q = \sqrt{3J_2} \quad (11)$$

where J_2 is the second invariant of the stress deviator tensor.

4. Numerical Model

In this study, the simulation is conducted on COMSOL Multiphysics 6.2. According to the geological setting gained from the logging data of the B unit, a geological model with a size of 200 m × 200 m × 100 m is set, buried 475 m underground from the top. It is assumed that the average density of the overlying strata is 2300 kg/m³. The geological properties used for the model are set in the Table 1.

Table 1. Basic rock properties for rock layers.

Lithology	Young's Modulus (GPa)	Poisson's Ratio	Density (kg/m ³)	Cohesion (MPa)	Angle of Internal Friction (deg)
Shale	25	0.35	2500	1.5	25
Salt	2.26	0.28	2200	5.76	31.6
Anhydrite	12.9	0.22	3000	3.2	35
Limestone	20	0.23	2700	15.9	36

The stress field of the model before caverns excavated is shown in the Figure 5.

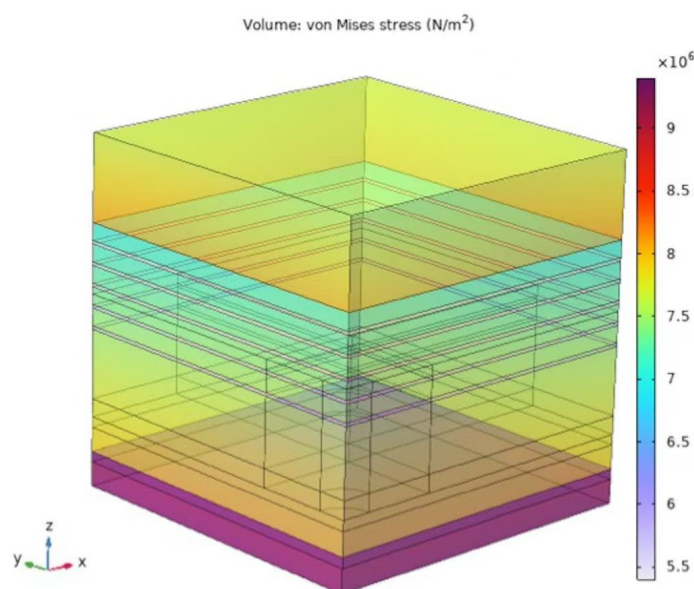


Figure 5. Geological model before the excavation of caverns.

4.1. Cavern Design

To investigate the effect of cavern shape and diameter on short-term stability, three different shapes of caverns were adopted for simulation: cylinder, cone, and ellipsoid. Each cavern type was modeled with a fixed height of 35 m, ensuring a suggested 20-meter-thick hanging wall and 10-meter-thick foot wall to maintain basic stability. For each shape, five diameters were selected: 17.5 m, 35 m, 52.5 m, 70 m, and 87.5 m, corresponding to the diameter–height ratios of 0.5, 1, 1.5, and 2. Models assume that 15% of insoluble sediment will be left in the bottom of cavern after leaching. Calculations for the height of sediments for each shape of caverns are as follows:

1. Cylinder

$$\pi r^2 h = 0.15 \pi r^2 H \quad (12)$$

$$h = 0.15H = 5.25 \text{ m} \quad (13)$$

2. Upside-Down Cone

Assuming the ratio between the parameter of the cone and height is a , the following is thus derived:

$$\frac{1}{3}\pi ah^3 = \frac{0.15}{3}\pi aH^3 \quad (14)$$

$$h = \sqrt[3]{0.15H} = 18.60 \text{ m} \quad (15)$$

3. Ellipsoid

To make the most of the underground space, the cross-section of the ellipsoid is set to be a circle. It is assumed that the ratio between the parameter of the ellipsoid and height is a . Thus, the equation of ellipsoid can be written as follows:

$$\frac{x^2}{a^2H^2} + \frac{y^2}{a^2H^2} + \frac{z^2}{H^2} = 1 \quad (16)$$

Setting the cross-section at half of the height of the ellipsoid as the coordinate system plane, the following is thus obtained:

$$\int_{-\frac{H}{2}}^{-(\frac{H}{2}-h)} \pi \left(1 - \frac{z^2}{H^2}\right) a^2 H^2 dz = 0.15 \frac{4}{3} \pi a^2 \frac{H^3}{8} \quad (17)$$

For $H = 35$ m, the equation leads to

$$h = 8.55 \text{ m} \quad (18)$$

4.2. Operating Pressure Design and Leakage Evaluation

Ensuring the long-term stability of salt caverns for underground hydrogen storage (UHS) requires careful consideration of operating pressures during repeated injection and withdrawal cycles. To maximize storage capacity in each cycle, the maximum internal pressure is expected to be as high as possible, while the minimum internal pressure is expected to be as low as possible to guarantee maximum hydrogen utilization. However, different pressure levels affect the stress field around the cavern, posing potential safety risks such as roof collapse, pillar damage, or gas leakage. According to previous studies [36,37], the gas pressure inside the cavern should be within the range between 30% and 85% of the vertical pressure on the cavern top to maintain cavern stability. Considering the presence of weak interlayers, choosing the appropriate operating pressure. Thus, this study adopts a maximum operating pressure of 0.8 times the vertical stress and a minimum operating pressure of 0.3 times the vertical stress initially. To determine the optimal operating pressure range and analyze the effect operation pressure has on the overall stability of the cavern, a stationary study of different operation pressures applied on the salt cavern is first conducted by applying the operating pressures of 0.3, 0.4, 0.5, 0.6, 0.7, and 0.8 times of the vertical stress, and the resulting deformation is analyzed to find out the impact operating pressure has on the stability of caverns. Following the mechanical analysis, a tightness evaluation is then performed to assess the risk of hydrogen leakage based on the preliminary result gained, as the operating pressure is the primary driving force for hydrogen diffusion. Considering typical energy supply–demand fluctuations and current hydrogen injection–extraction technology, a conservative cycle frequency of four times per year is assumed. The simulation runs for 10 years to estimate the total leakage rate, providing insights into the long-term performance and safety of the storage system.

5. Modeling Results

5.1. Cavern Shape and Parameters Optimization

The modified stress field and displacement after the cavern leaching can be crucial when deciding the appropriate shape and parameter for UHS, as both excessive stress and displacement can compromise the integrity of salt caverns and put the whole system in threat. Therefore, selecting the optimal cavern shape helps keep the maximum stress in a resealable range, introducing relatively small displacement and resulting in little or no plastic zone. After the construction of the caverns, the stress field and displacement cloud atlas are as follows:

1. Cylinder

Cylinder-shaped caverns are set with diameters of 0.5, 1, 1.5, and 2 times its height. After excavation, the von Mises stress fields are shown in Figure 6.

From the von Mises stress distribution map, stress concentration is primarily observed in the embedded shale layers around the caverns and at the edges of the top and bottom of cylindrical-shaped caverns. The maximum von Mises is generally located at the edge of the cavern roof in the direction of the maximum horizontal stress (x -axis direction), except for caverns with a diameter–height ratio of 0.5, indicating roof edge will be mostly threatened by the risks of instability, where fractures may develop perpendicular to the direction of the maximum horizontal stress.

In addition, the maximum von Mises stress occurs in the embedded shale layers for caverns with a ratio of 0.5, indicating that weak embedded shale layers significantly influence cavern stability by introducing stress concentrations. However, as the diameter increases, von Mises stress grows more dramatically on the edge of the upper roof, making it the most critical point for potential failure.

According to the maximum von Mises stress curve, the stress grows steadily with the diameter-to-height ratio until the diameter approaches twice the height. This suggests that the salt rock near the cavern roof reaches its loading limit at a diameter-to-height ratio close to 2, highlighting a critical threshold for maintaining cavern stability.

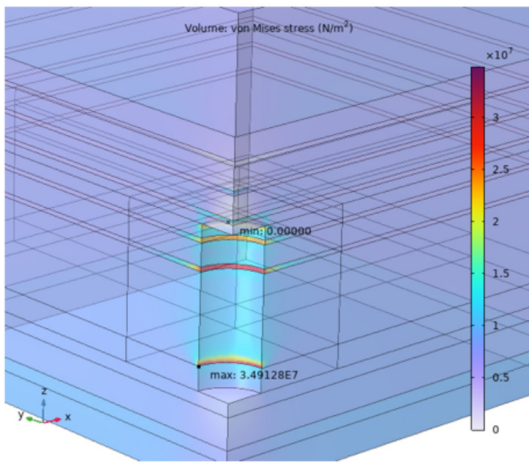
Apart from stress, displacement contour plots of different caverns are shown below.

Figure 7 demonstrates that after leaching, both the top and bottom of the cavern tend to deform. The cavern roof bends downward, while the cavern floor protrudes upward. Additionally, the sidewalls bend inward slightly. Though these displacements remain minor when the diameter is rather small, the roof displacement increases significantly as the diameter-to-height ratio grows, while floor protrusion and sidewall bending remain relatively stable within a range of 0.005 m to 0.006 m.

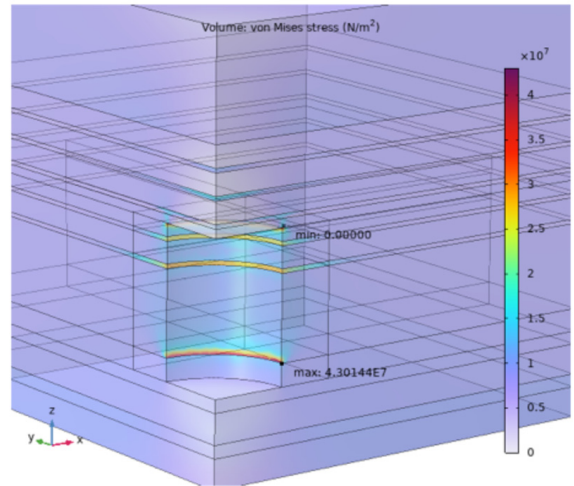
Moreover, As the cavern diameter increases, the deformation region expands, and the displacement contour can extend beyond the simulated strata when the diameter-to-height ratio exceeds 1. The maximum displacement point can be found at the center of the top roof, increasing linearly to 0.18 m when the diameter-to-height ratio reaches 2. The linear growth of the maximum displacement suggests that salt rock on the central part of the roof is still within the elastic range, but it does not guarantee the overall stability of the cavern as the maximum displacement becomes too large, imposing potential danger to the system.

Furthermore, the embedded shale layers show no significant difference in displacement compared to the surrounding salt rock, indicating that the cavern's sidewall surface remains continuous after excavation, reducing the risk of fractures or misalignment around these weak layers.

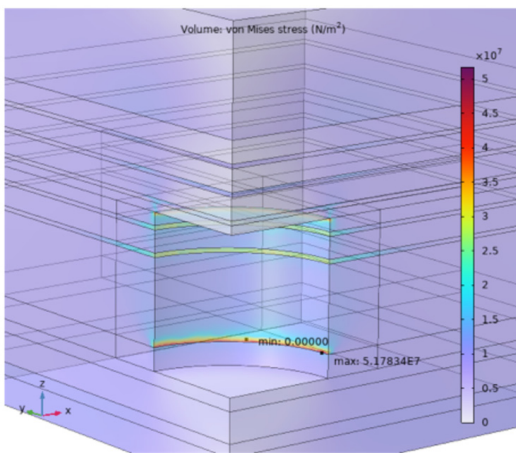
To better find out how the plastic region grows, the plastic strain cloud plots are presented in Figure 8.



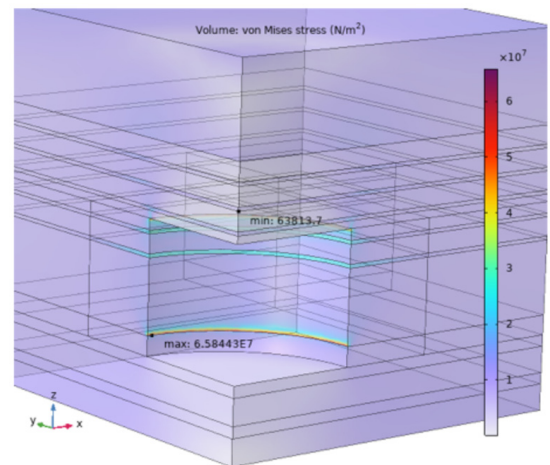
(a)



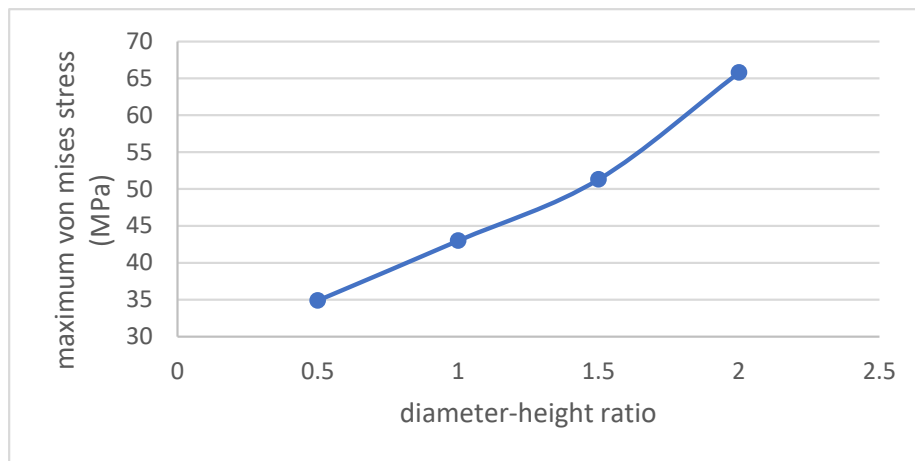
(b)



(c)

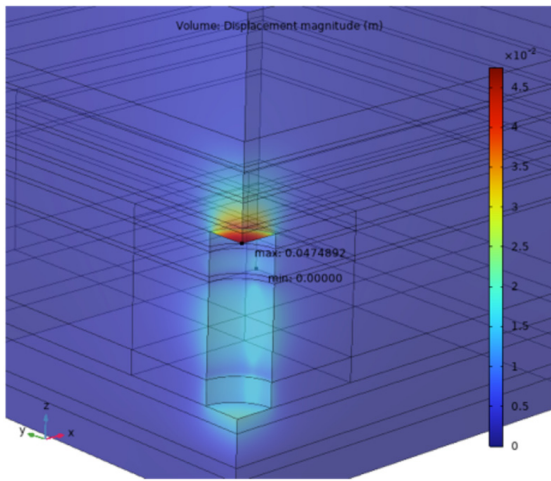


(d)

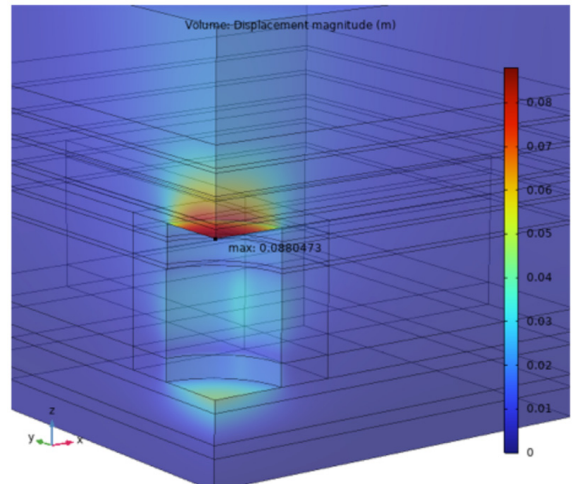


(e)

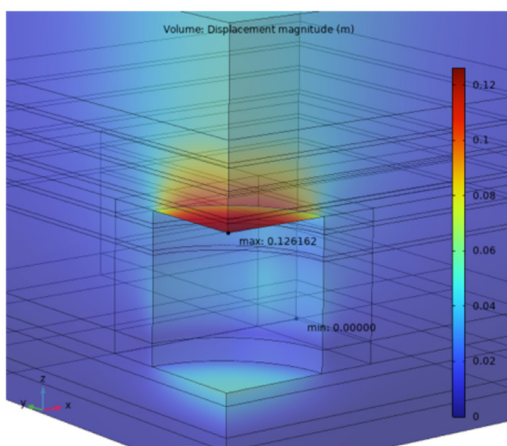
Figure 6. Stress field after cylinder-shaped caverns with different diameter–height ratios excavated, (a) ratio = 0.5, (b) ratio = 1, (c) ratio = 1.5, (d) ratio = 2.0, (e) maximum von Mises stress curve corresponding to different ratios.



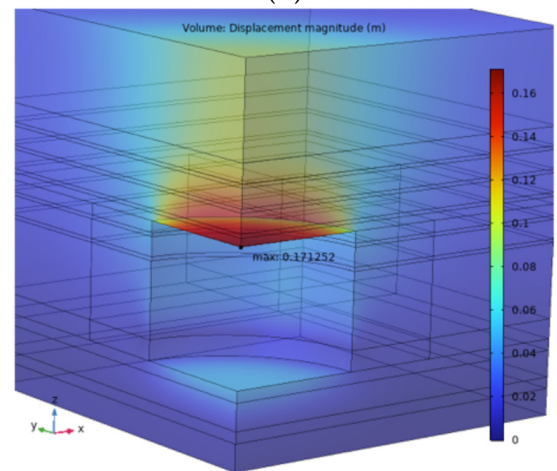
(a)



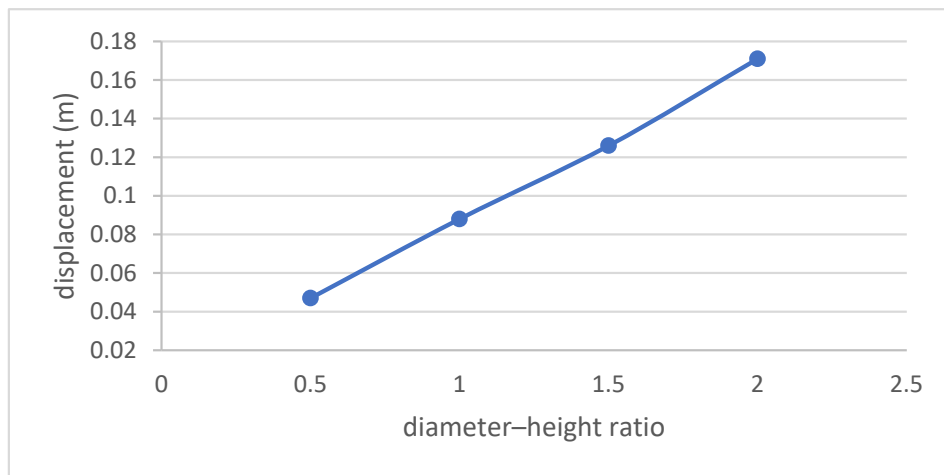
(b)



(c)



(d)



(e)

Figure 7. Displacements after cylinder-shaped caverns with different diameter–height ratios excavated, (a) ratio = 0.5, (b) ratio = 1, (c) ratio = 1.5, (d) ratio = 2.0, (e) maximum displacement curve corresponding to different ratios.

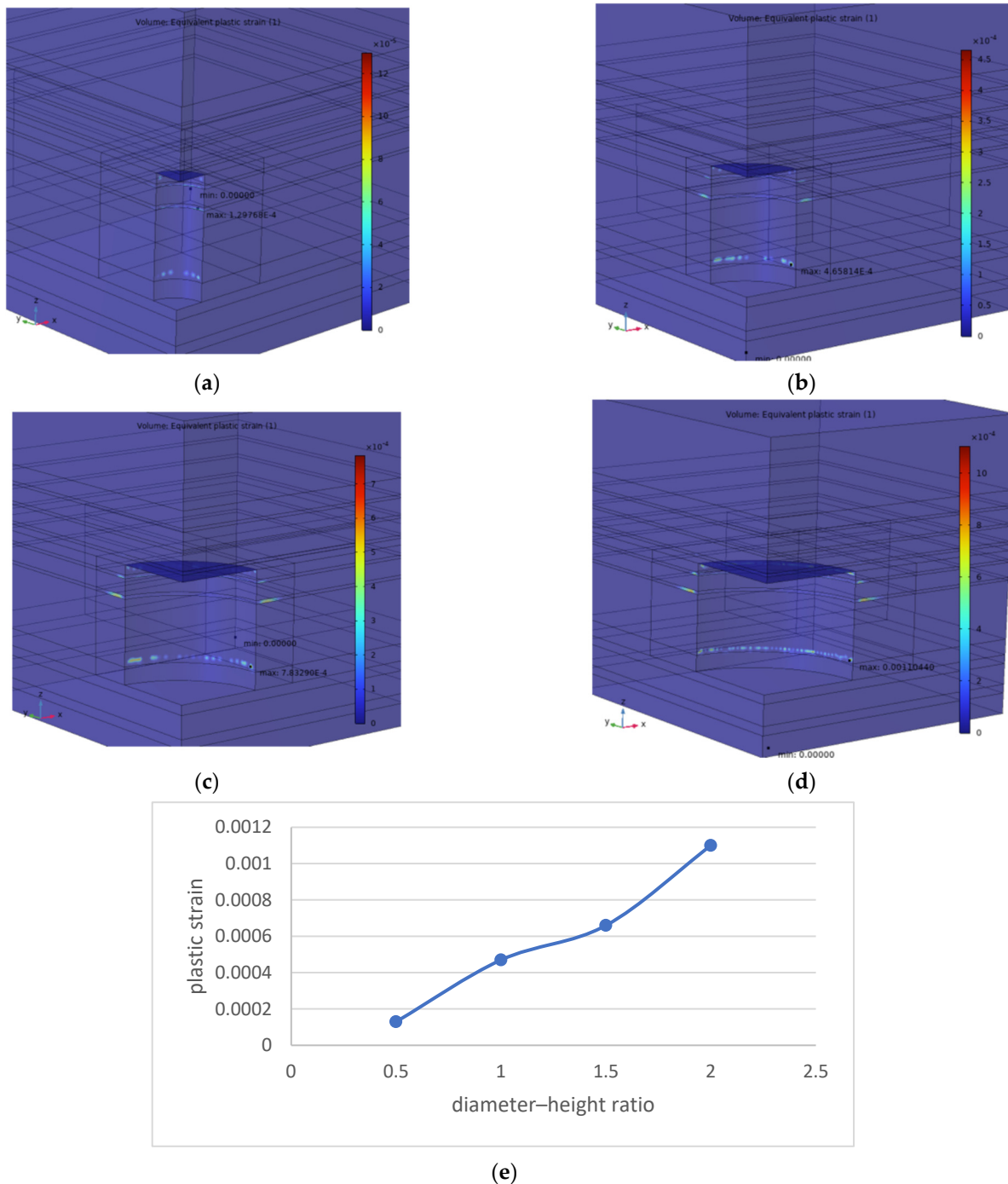


Figure 8. Plastic strain after cylinder-shaped caverns with different diameter–height ratios excavated, (a) ratio = 0.5, (b) ratio = 1, (c) ratio = 1.5, (d) ratio = 2.0, (e) maximum plastic strain curve corresponding to different ratios.

Figure 8 represents the development of the plastic zone around the cavern as the diameter increases. It is shown that the plastic zone primarily forms in four areas: salt rocks near the cavern sidewalls close to the roof, two embedded shale layers, and salt rocks near the cavern sidewalls close to the floor. When the diameter reaches twice the height, small regions at the edges of the cavern, particularly within the embedded shale layers, begin to exhibit plastic deformation, indicating that displacement and stress fields induced by larger diameters can trigger plastic deformation further from the cavern, bringing greater potential risks and harming the integrity of the system.

The maximum plastic strain varies with cavern diameter but predominantly occurs within the embedded shale layers, highlighting that these weak layers reduce the cavern's resistance to deformation. The maximum plastic strain generally increases linearly with diameter but has a slight acceleration when the ratio is below 1.5. As the ratio approaches 2, the rate of increase slows, indicating the system is nearing instability.

In summary, when the shape is settled to the cylinder, the best diameter may be set to 1.5 to 2 times its height in unit B.

2. Upside-Down Cone

Changes in cavern shape significantly influence the stress field and displacement patterns. However, despite the numerical differences, the overall distribution remains consistent: stress concentration is primarily located at the edges of the roof and within the embedded shale layers, and displacement is concentrated in the central part of the top roof. To streamline this article, the detailed cloud maps of these properties are omitted. Instead, only the maximum values and their corresponding curves are presented to illustrate the key findings succinctly.

Figure 9 demonstrates the correlation between the maximum von Mises stress and the diameter–height ratio.

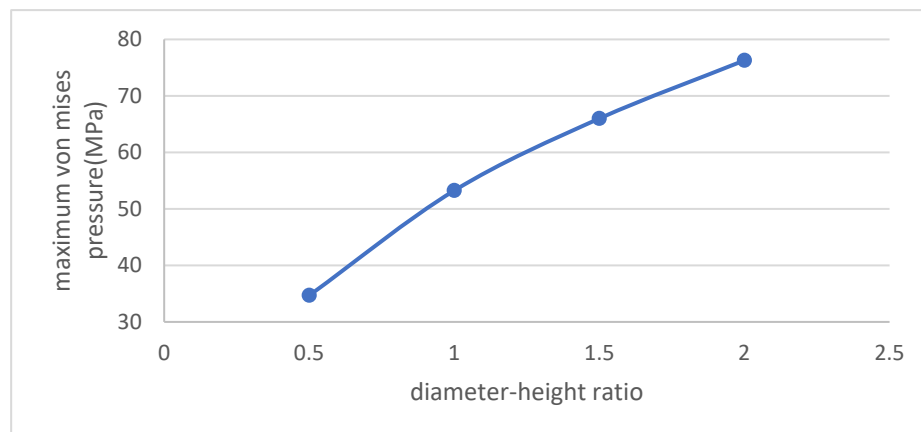


Figure 9. Maximum von Mises stress curve corresponding to different ratios.

As the cavern diameter increases, the maximum von Mises stress rises significantly, with a sharper increase when the diameter-to-height ratio reaches 2. The maximum stress consistently occurs at the edges of the upper roof and is notably higher in cone-shaped caverns compared to cylindrical caverns of the same diameter. This is due to the much thinner edge of the cone top, making stress concentration much more likely to occur and much more intense. Such high stress levels are undoubtedly harmful to the overall stability of the cavern. It is noteworthy that in practice, leaching processes rarely produce a perfectly inverted cone shape. Thus, the extremely thin edges that exacerbate stress concentration might not form, but the angle between the roof and sidewalls in cone-shaped caverns still increases the risk of stress concentration, making this geometry less favorable for maintaining structural integrity.

In addition, the maximum displacements formed in the cone-shaped caverns and the induced plastic strain are shown in Figures 10 and 11.

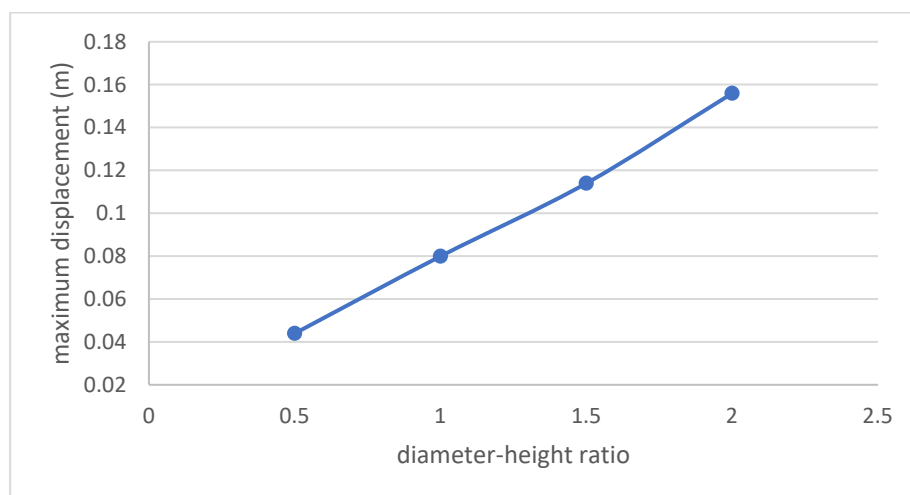


Figure 10. Maximum displacement curve corresponding to different ratios.

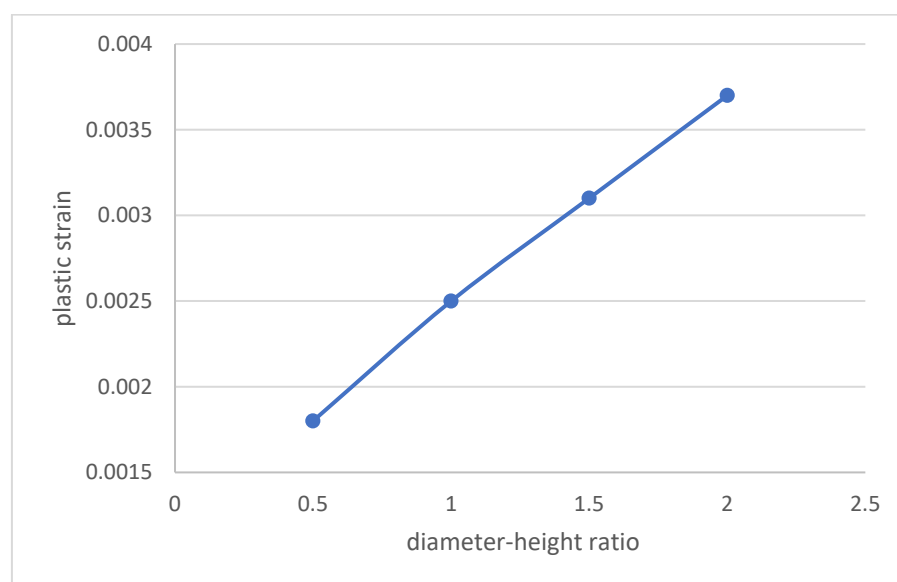


Figure 11. Plastic strain curve corresponding to different ratios.

According to the curve, all three variables—maximum von Mises stress, maximum displacement, and maximum plastic strain—increase with cavern diameter. Like the cylinder-shaped cavern, the maximum displacement is found in the central part of the roof, and the maximum plastic strain occurs within the embedded shale layers.

However, in cone-shaped caverns, both the maximum von Mises stress and plastic strain are significantly higher than in cylindrical caverns of the same diameter, as the intensified stress concentration at the thinner roof edges largely affects the stability of cone-shaped caverns, indicating a higher risk of failure. These findings demonstrate that cone-shaped caverns are subject to greater potential hazards compared to cylindrical caverns, making them a less favorable option for underground hydrogen storage.

3. Ellipsoid

The stress field and displacement distribution in ellipsoid-shaped caverns differ from those in cylindrical and cone-shaped caverns due to the smooth surface of the ellipsoid, which reduces the likelihood of stress concentration. However, a consistent distribution pattern can be found with the change in diameter. To maintain conciseness, caverns with diameter–height ratios of 1.0 and 1.5 are illustrated as examples. Figure 12 shows the stress

distribution of these two examples and the correlation between the maximum von Mises stress and the diameter–height ratio.

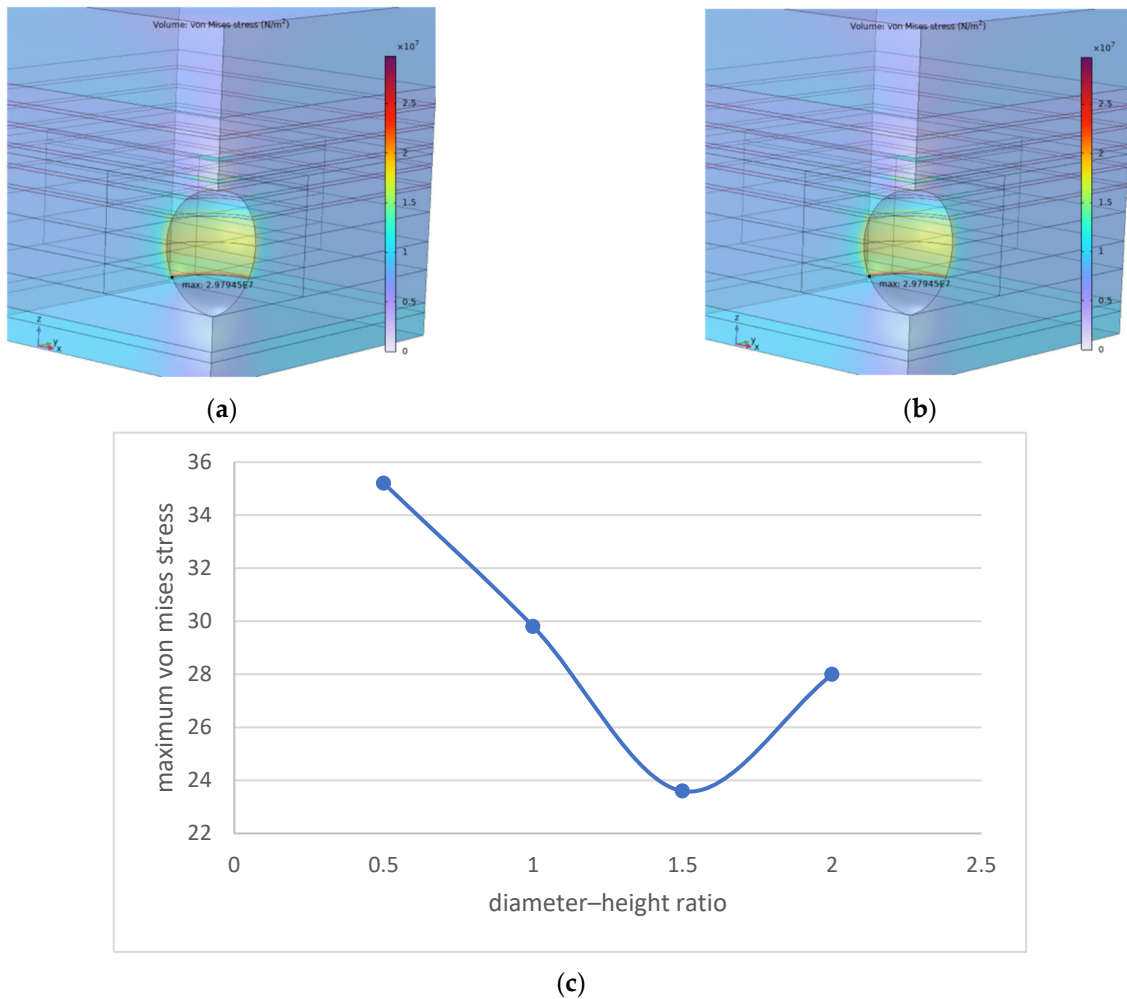


Figure 12. Von Mises stress after ellipsoid-shaped caverns with different diameter–height ratios excavated, (a) ratio = 1.0, (b) ratio = 1.5, (c) maximum von Mises stress curve corresponding to different ratios.

The von Mises stress cloud plots show that stress concentration in ellipsoid-shaped caverns mainly occurs in two regions: the edge around the sediment top surface and the middle section of the sidewall. Before the diameter–height ratio reaches around 1.5, stress concentration near the sediment edge is more prominent. As the ratio increases beyond 1.5, the primary stress concentration shifts toward the middle of the sidewall, although the sediment edge continues to experience higher pressure compared to the surrounding salt rock. Moreover, like cylinder- and cone-shaped caverns, there is an uneven stress distribution between the embedded shale layers and the surrounding salt rock.

Apart from the von Mises stress distribution, another notable difference is the trend in maximum von Mises stress with increasing diameter. When the diameter-to-height ratio is below 1.0, the maximum von Mises stress is found near the sediment edge. Then, as the diameter continues to grow, the maximum stress occurs around the embedded shale layers. Unlike cylinder- and cone-shaped caverns, the maximum von Mises stress in ellipsoid-shaped caverns decreases significantly when the ratio is between 0.5 and 1.0, but increases dramatically afterwards, making the maximum von Mises stress significantly lower when the ratio is 1.0 than that of other conditions. In addition, the maximum von Mises stress is the lowest among caverns with all three shapes under the same condition,

and the difference reaches its most when the diameter–height ratio is 1.0. It is noteworthy that the dramatic increase after the ratio reaches 1.5 makes the cavern reach instability rapidly with the continuous growth in diameter, so when the ratio reaches 2.0, the cavern reaches its stability limit.

Figures 13 and 14 illustrate the displacement and plastic strain distribution after cavern leaching. The displacement pattern is consistent with that seen in cylindrical and cone-shaped caverns: the upper roof bends downward, while the bottom floor protrudes upward. The largest displacement is concentrated in the upper roof. Although the maximum displacement generally increases with the diameter-to-height ratio, it shows a slight drop when the ratio reaches 1.5.

The plastic strain distribution also follows a similar trend to the other cavern shapes, increasing with the diameter-to-height ratio and primarily occurring within the embedded shale layers. Additionally, minor plastic deformation develops in the weak shale layer above the cavern when the ratio reaches 1.0. Despite these trends, both the maximum displacement and maximum plastic strain in ellipsoid-shaped caverns are lower compared to cylindrical and cone-shaped caverns under the same conditions.

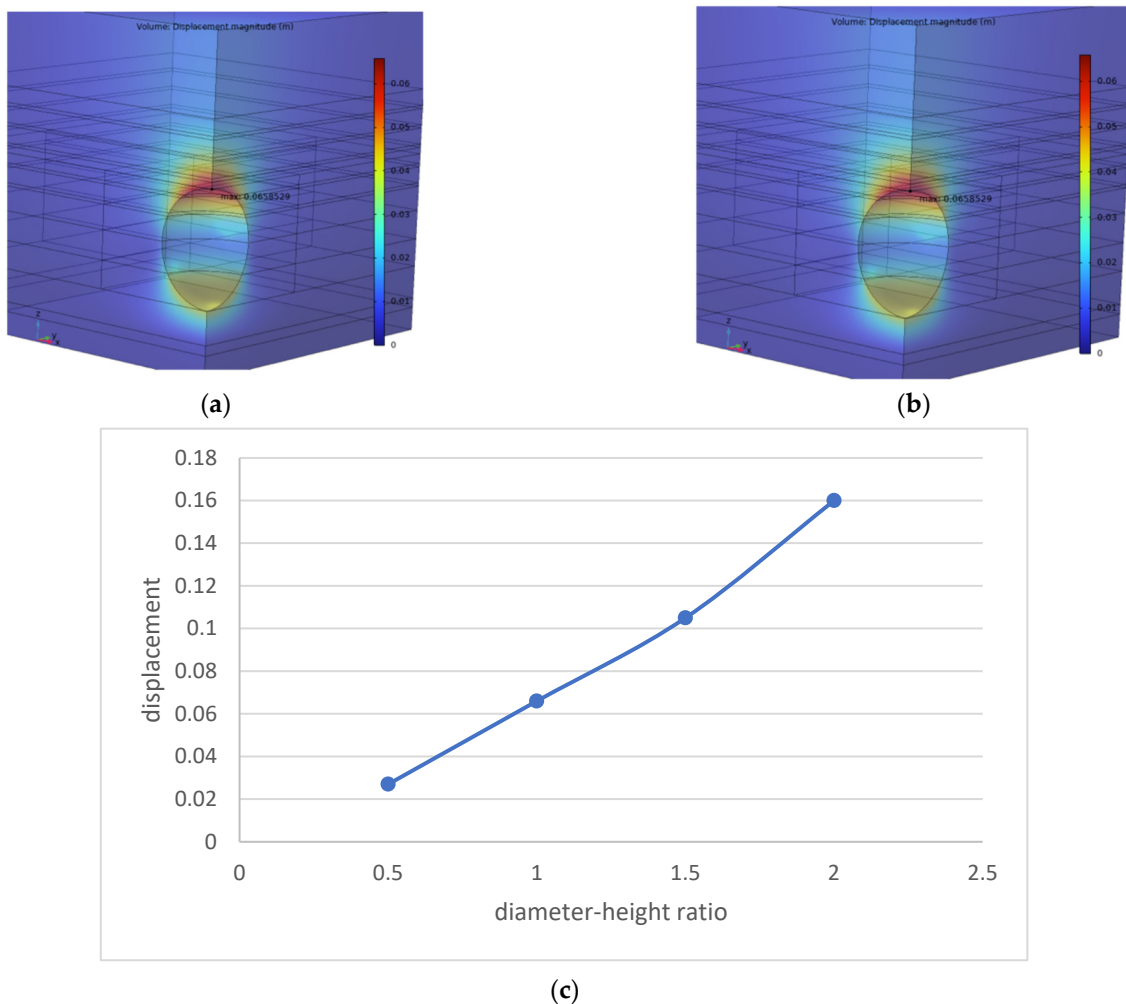


Figure 13. Displacement after ellipsoid-shaped caverns with different diameter–height ratios excavated, (a) ratio = 1.0, (b) ratio = 1.5, (c) maximum von Mises stress curve corresponding to different ratios.

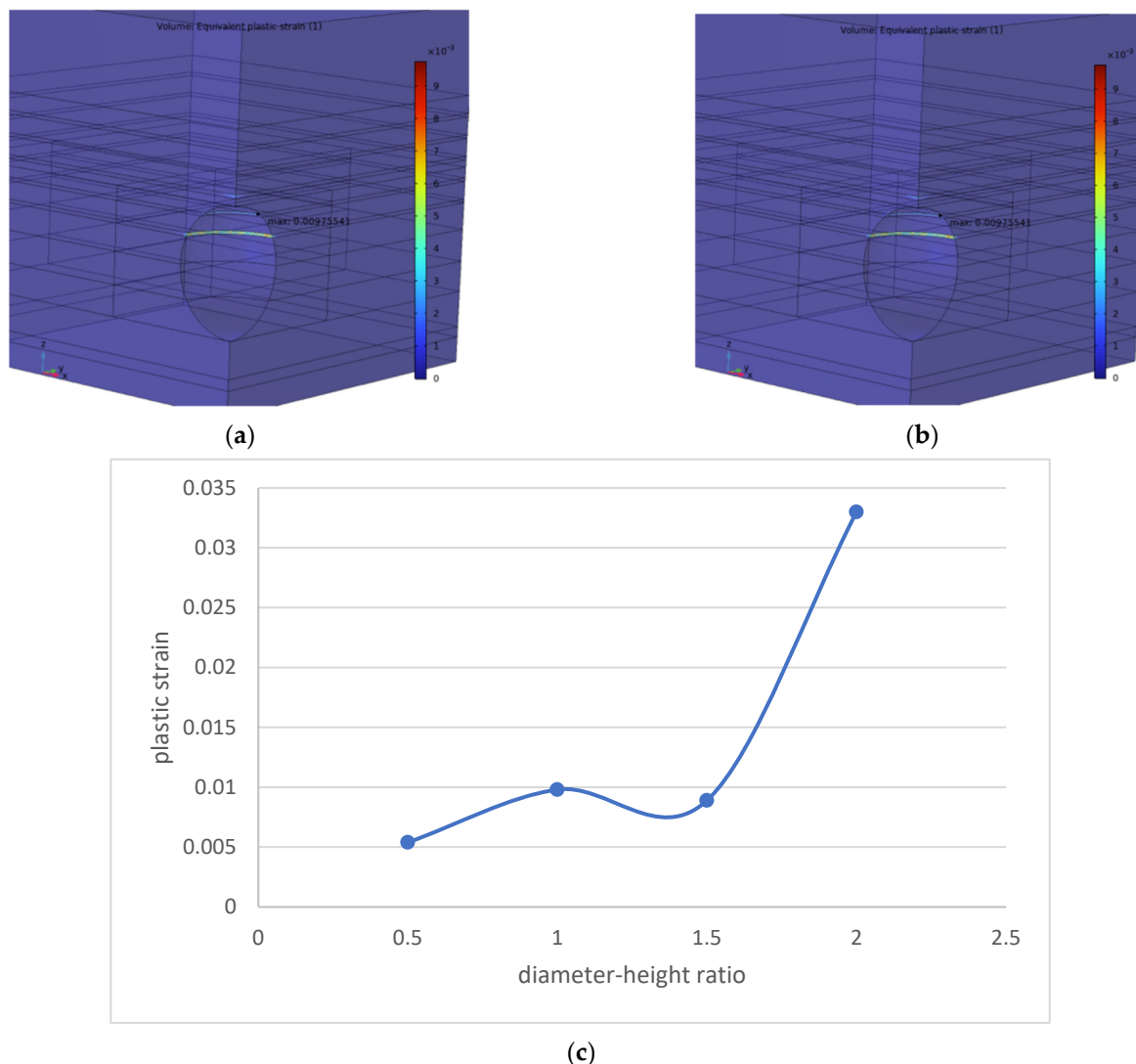


Figure 14. Plastic strain after ellipsoid-shaped caverns with different diameter–height ratios excavated, (a) ratio = 1.0, (b) ratio = 1.5, (c) maximum von Mises stress curve corresponding to different ratios.

Though the cavern with the shape of an ellipsoid has a more stable structure when the ratio is below 1.5, its smaller volume compared to a cylinder-shaped cavern makes it less competitive.

Considering the findings discussed above, this study identifies the cylindrical cavern with a diameter-to-height ratio of 1.5 as the most suitable option for underground hydrogen storage. While ellipsoid-shaped caverns show promising stability due to reduced stress concentration and displacement, their shape is difficult to control during leaching, and their storage capacity is comparatively limited. Therefore, the cylindrical cavern offers a balance between structural stability and storage capacity, making it the preferred choice for practical implementation.

5.2. Long-Term Stability

5.2.1. Impact of Operating Pressure

After applying different operating pressures to the cavern wall, the distribution of von Mises stress and plastic strain is shown in Figures 15 and 16. To keep the article concise, contour plots are presented for pressures of 0.4, 0.6, and 0.8 times the vertical stress, as the distributions exhibit a consistent pattern across the range of pressures.

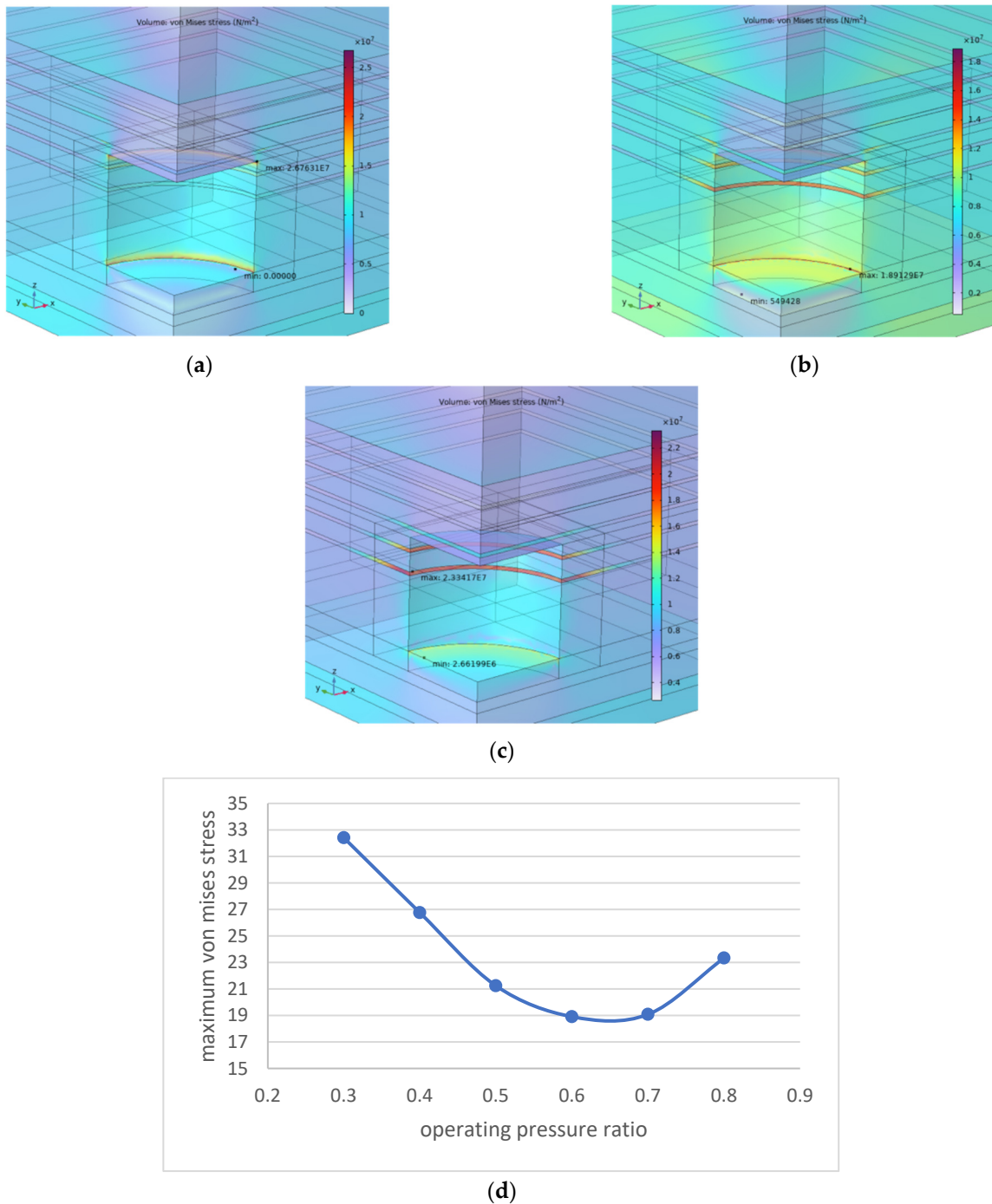


Figure 15. Von Mises stress distribution at different operating pressure to vertical stress ratio, (a) ratio = 0.4, (b) ratio = 0.6, (c) ratio = 0.8, (d) maximum von Mises stress curve corresponding to different ratios.

For stress distribution, it is demonstrated that with increasing operating pressure, the stress distribution follows a consistent pattern, forming stress concentrations at the edges of the cavern roof and floor as well as within the embedded shale layers. This distribution is similar to the stress pattern observed immediately after excavation.

The maximum von Mises stress initially decreases and then increases once the pressure ratio reaches 0.6. This occurs because, after the initial excavation, the surrounding rock compresses the cavern. Moderate operating pressures help to counterbalance this compression, reducing the stress on the cavern walls. However, once the operating pressure

exceeds the natural compression of the rock, the walls experience renewed compression, causing the stress to rise again.

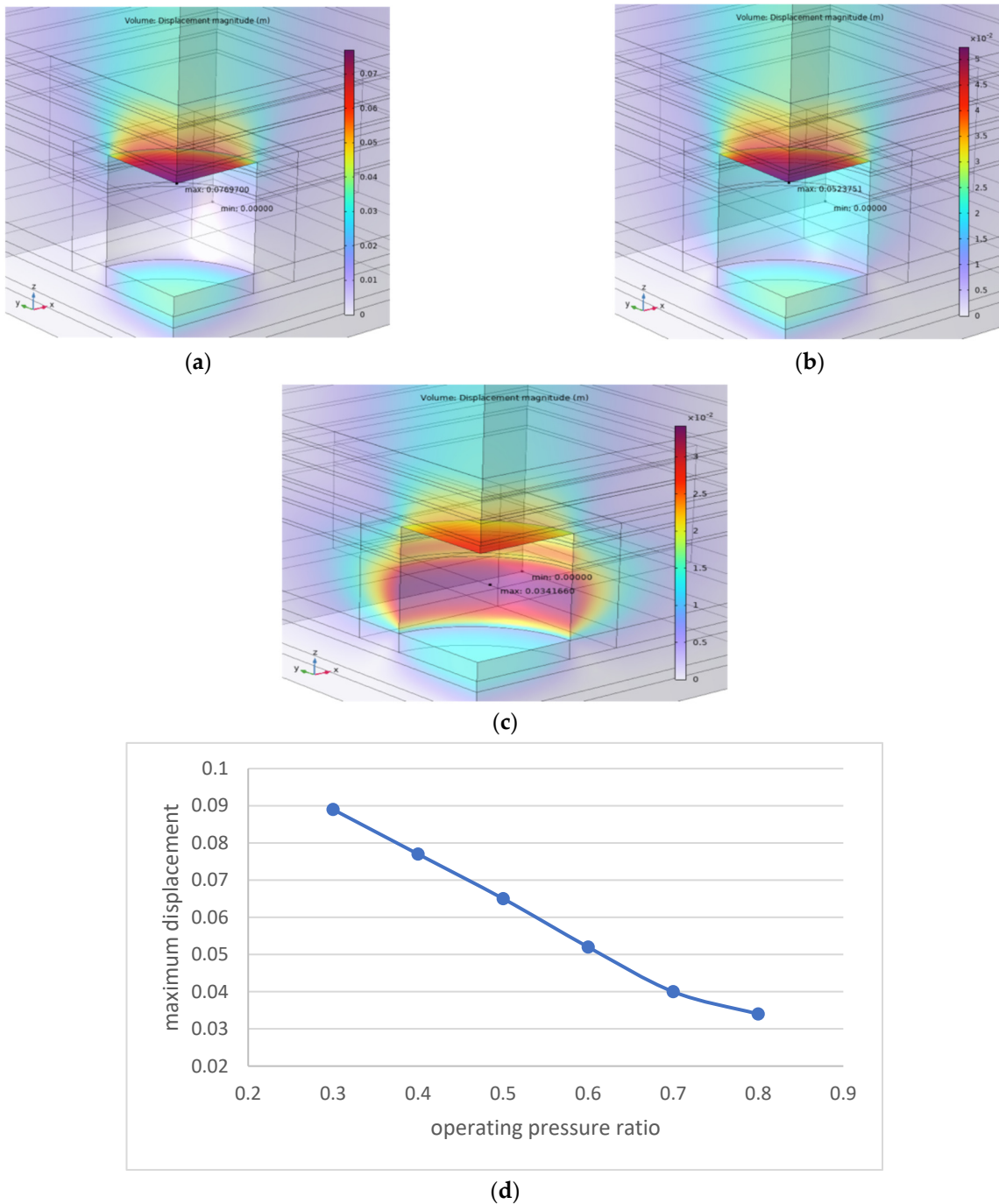


Figure 16. Displacement distribution at different operating pressure to vertical stress ratio, (a) ratio = 0.4, (b) ratio = 0.6, (c) ratio = 0.8, (d) maximum displacement curve corresponding to different ratios.

As the operating pressure increases, stress concentration within the shale layers intensifies, becoming particularly pronounced when the pressure ratio exceeds 0.7. This is due to the greater deformability of the salt rock compared to the shale. Under higher pressure, the salt rock tends to expand outward more than the shale layers. This differential movement imposes shear stress on the shale interlayers, amplifying stress concentration.

This phenomenon poses a risk to the long-term stability of the hydrogen storage system, as excessive shear stress can lead to potential slippage or fractures between the salt rock

and shale interlayers. Careful management of operating pressure is essential to mitigate these risks and maintain cavern integrity over extended injection and withdrawal cycles.

For displacement, the maximum displacement decreases as the operating pressure increases, with the rate of decrease slowing when the pressure ratio reaches 0.7. This suggests that at higher operating pressures, the surrounding rock becomes over-compressed, reducing its capacity to deform and increasing the likelihood of fractures, which can compromise cavern stability.

When the operating pressure is around 0.4 times the vertical stress, the cavern wall remains close to its original design shape. At this pressure, the deformation caused by the operating pressure effectively offsets the compression from the surrounding strata. However, as the operating pressure continues to rise, the cavern wall tends to expand outward, causing a displacement difference between the salt rock and the embedded shale layers due to the salt rock's greater softness. This effect is most pronounced when the pressure ratio reaches 0.8.

Interestingly, the plastic zone does not change with varying operating pressure and remains consistent with the conditions observed right after the cavern's construction. This indicates that the creep behavior of the salt rock, rather than operating pressure, is the dominant factor driving plastic deformation.

Based on these stationary simulations, the optimal minimum operating pressure is around 0.4 times the vertical stress, while the maximum operating pressure should be kept below 0.8 times the vertical stress to ensure long-term cavern stability and integrity.

5.2.2. Leakage Evaluation

Although salt caverns have low leakage potential due to their low porosity and permeability, evaluating cavern tightness is essential. Operating pressure is a key factor affecting overall tightness. To simulate this effect, a minimum operating pressure of 0.4 times the vertical stress is applied, while the maximum operating pressures are set at 0.6, 0.7, and 0.8 times the vertical stress.

The simulation period is set to 10 years, with four injection–withdrawal cycles per year, to assess potential hydrogen leakage over time. The relevant rock properties are shown in Table 2.

Table 2. Percolation properties for rock layers.

Lithology	Permeability (m ²)	Porosity	Compressibility	Diffusion Coefficient (m ² /s)
Shale	1×10^{-19}	0.07	3.6×10^{-11}	1×10^{-9}
Salt	1×10^{-21}	0.01	5.84×10^{-10}	1×10^{-10}
Anhydrite	1×10^{-19}	0.04	1.3×10^{-10}	1×10^{-9}
Limestone	1×10^{-18}	0.01	1×10^{-10}	1×10^{-9}

Considering the dense nature of the surrounding rock, the initial pore pressure around the cavern is set to 0. After a 10-year simulation, the resulting pore pressure distribution reveals the extent of hydrogen leakage and diffusion. It is noteworthy that though leakage will also occur in injection and extraction wells, such leakage can be neglected due to the small volume of the well compared to the salt rock deposit. Figure 17 illustrates the pore pressure distribution after 10 years. Since the distribution follows a consistent pattern, only the case where the pressure ratio is 0.6 is shown as an example.

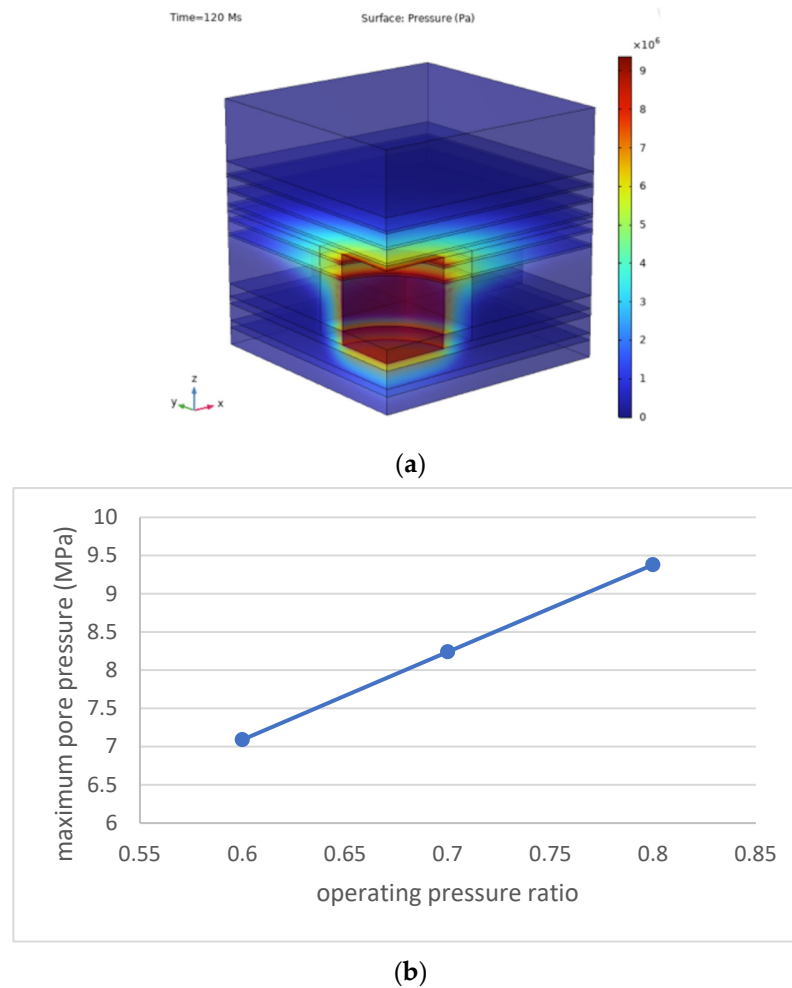


Figure 17. Pore pressure distribution at the end of simulation, (a) ratio = 0.6, (b) maximum pore pressure curve corresponding to different ratios.

The pore pressure distribution shows that hydrogen dissipates into the surrounding rock from all parts of the cavern, with the greatest diffusion occurring within the embedded shale layers, leading to higher hydrogen leakage in these regions. The pore pressure remains relatively uniform around the cavern, except in the shale layers, where it is significantly higher than in the adjacent salt rock. This indicates an accumulation of leaking hydrogen within the shale layers. Additionally, hydrogen that dissipates into the shale layers tends to infiltrate nearby salt rock, expanding the overall diffusion area.

Although the hydrogen dissipation pattern remains consistent across different maximum operating pressures, the maximum pore pressure increases linearly with the maximum operating pressure, suggesting greater hydrogen loss at higher pressures.

To comprehensively evaluate the storage performance, both the hydrogen diffusion area and the leakage rate relative to the gas storage capacity should be assessed.

The gas storage capacity is influenced by factors such as cavern shape, operating pressure, and injection–extraction frequency. The gas storage capacity for one injection–production cycle can be calculated using the following formula:

$$M = n \frac{M_{H_2} V_0}{R} \left(\frac{P_{\max}}{Z_1 T_1} - \frac{P_{\min}}{Z_2 T_2} \right) \tag{19}$$

where M is the working hydrogen mass of hydrogen in kg. M_{H_2} is the molar mass of hydrogen. V_0 is the cavern volume, and R is the gas constant, set to 8.314 J/(Mol·K). Z is the compression factor of the actual hydrogen. T is the temperature in K, assuming that

the temperature of surrounding rock stays the same during the whole process and the hydrogen was injected with the same temperature as the surrounding strata. T was set to be 303.15 K, an average value for strata 500 m beneath. n is the number of cycles taken for 10 years. The simulation lasts for 10 years, and each year takes 4 cycles, making 40 cycles in total.

After the simulation, the working gas capacity and the total mass of leaked hydrogen are shown by Table 3 and Figure 18.

Table 3. Total hydrogen capacity and leakage rate.

Operating Pressure (MPa)	Capacity (kg)	Total Mass of Leaked Hydrogen (kg)	Leakage Rate (%)
4.8–9.6	1×10^7	174,968	1.74
4.8–8.4	7.71×10^6	171,944	2.23
4.8–7.2	5.28×10^6	169,924	3.22

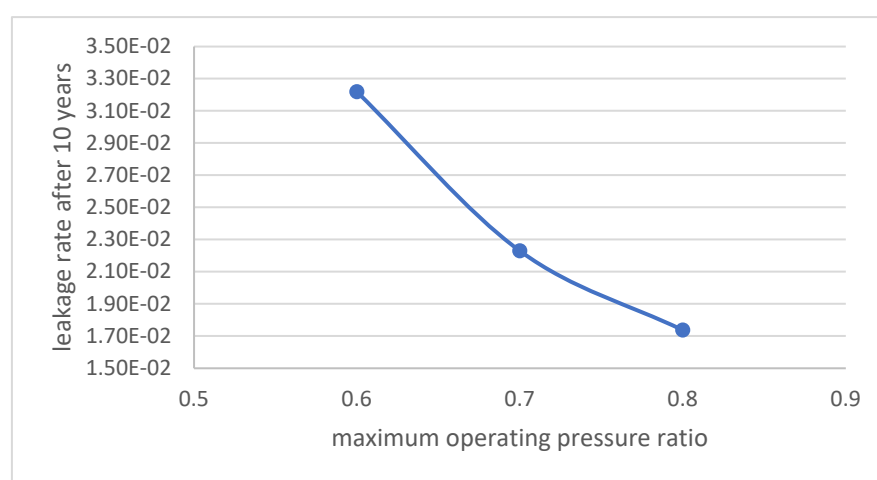


Figure 18. Leakage rate after 10 years.

The results indicate that as the maximum operating pressure increases, the hydrogen leakage rate decreases. This is due to the low permeability of the surrounding rock, which slows down the diffusion of hydrogen. With the increase in the maximum operating pressure, the total leakage mass of hydrogen rises, but is rather slow compared to the increment in total gas stored due to the difficulty of percolation, causing the leakage rate to drop. However, the decrease in leakage rate is more pronounced when the maximum operating pressure increases from 0.6 times to 0.7 times the vertical stress than it is between 0.7 times and 0.8 times. This suggests that while higher operating pressures contribute to hydrogen leakage, the effect diminishes at higher pressure ratios. Nevertheless, higher maximum operating pressures also pose risks to cavern stability, as greater stresses and displacements are imposed on the cavern walls.

Therefore, setting the maximum operating pressure to around 0.7 times the vertical stress strikes a balance between minimizing leakage and maintaining structural stability of the cavern.

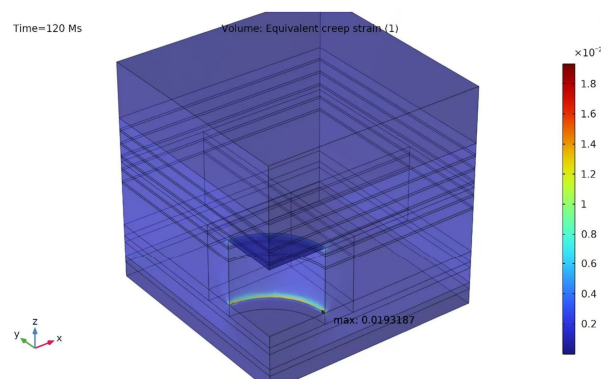
5.2.3. Creep Evaluation

Creep behavior is another critical characteristic of salt rock that can compromise its long-term integrity after prolonged injection–extraction cycles. To ensure the long-term stability of the cavern under the designed operation pressure range of 0.4 to 0.7 times of vertical stress, creep simulation is conducted under the same working condition over a 10-year period. The relevant rock properties are shown in the Table 4.

Table 4. Creep properties for rock layers.

Lithology	Creep Rate Coefficient (1/s)	Stress Exponent	Reference Stress (Mpa)
Shale	5×10^{-15}	3.24	1.0
Salt	1.415×10^{-14}	3.52	1.0
Anhydrite	3.3×10^{-15}	3.16	1.0
Limestone	4.8×10^{-15}	4	1.0

Figure 19 demonstrates the equivalent creep strain distribution after the 10-year simulation.

**Figure 19.** Equivalent creep strain distribution after 10 years.

The equivalent creep strain distribution reveals that creep strain intensifies at the edges of both the upper roof and the bottom floor of the cavern, primarily due to stress concentrations caused by the sharp corners of the simulated cavern, and the maximum creep strain can be found on the edge of lower floor, as the lower depth of the bottom floor brings higher stress levels. The overall creep-affected area remains confined within a small region around the cavern, with most of the cavern walls showing minimal creep tendency, as the average creep strain is around 0.2% according to the graph, implying overall stability after a 10-year simulation. Though the maximum creep strain of 1.9% may pose potential danger to the salt cavern, perfect cylinder-shaped caverns with sharp edges are not common, and a curved surface is most likely formed during leaching; thus, the stress concentration is reduced and leads to a smaller maximum creep strain.

6. Conclusions

Based on the stratigraphy characteristics of the B unit of the Salina Group in south Canada, simulations have been performed to evaluate the feasibility and stability of underground hydrogen storage (UHS) in salt caverns, focusing on different cavern shapes, geometric parameters, and operating pressures. The leaching method can form three basic cavern shapes: cylinder, upside-down cone, and ellipsoid, and different diameters are applied when analyzing each shaped cavern's stability. The findings indicate that cylindrical caverns with a diameter-to-height ratio of 1.5 offer the best balance between storage capacity and structural stability and have the biggest storage potential. While ellipsoid-shaped caverns exhibit lower stress concentrations and displacements, their shape is difficult to control during leaching, and the innate small storage volume limits their practical application.

Simulations of different operating pressures revealed that the optimal pressure range lies between 0.4 and 0.7 times the vertical stress. At this range, the system maintains structural integrity while maintaining the hydrogen leakage at a reasonable value, and the relatively low creep strain also implies its long-term stability. Although higher pressures

increase storage capacity, they also lead to greater stress on cavern walls and higher leakage rates, compromising long-term stability.

This study also showed that hydrogen diffusion primarily occurs in embedded shale layers, which act as weak points for potential leakage. The plastic zone distribution remained largely unchanged with operating pressure, indicating that stationary analysis may not be sufficient, and the creep behavior of salt rock is the dominant factor for long-term deformation.

However, while this study conducted a 10-year simulation on the cavern's creep deformation, the creep analysis stays preliminary. The repeated injection and withdrawal cycles introduce both creep and fatigue effects that may gradually weaken the cavern structure [27]. Only considering the creep factor may lead to an incomplete understanding of the cavern's behavior during prolonged operations. Future studies should incorporate creep and fatigue simulations to provide a more comprehensive assessment of the long-term performance and safety of hydrogen storage in salt caverns.

Overall, this study presents a preliminary design for a UHS system in salt caverns located in southern Ontario, Canada, serving as a foundational step in this area of research. Future studies will include field experiments to obtain more precise geographical and geological data, validate the proposed design, and address practical aspects such as the economic impact and broader applications of the system. These efforts aim to provide a more comprehensive and reliable feasibility assessment.

Author Contributions: Writing, J.H.; supervision, S.Y. All authors have read and agreed to the published version of the manuscript.

Funding: This research received no external funding.

Data Availability Statement: The data that support the findings of this study are available from the co-authors upon request.

Acknowledgments: Mitacs, Origin Geomechanics Inc. and anonymous reviewers are greatly acknowledged.

Conflicts of Interest: The authors declare no conflicts of interest.

References

1. Zhang, Y.; Lebedev, M.; Sarmadivaleh, M.; Barifcani, A.; Rahman, T.; Iglauer, S. Swelling Effect on Coal Micro Structure and Associated Permeability Reduction. *Fuel* **2016**, *182*, 568–576. [CrossRef]
2. Sen, S.; Ganguly, S. Opportunities, Barriers and Issues with Renewable Energy Development—A Discussion. *Renew. Sustain. Energy Rev.* **2017**, *69*, 1170–1181. [CrossRef]
3. Elberry, A.M.; Thakur, J.; Veysey, J. Seasonal Hydrogen Storage for Sustainable Renewable Energy Integration in the Electricity Sector: A Case Study of Finland. *J. Energy Storage* **2021**, *44*, 103474. [CrossRef]
4. China's Wind and Solar Power Utilization Rates Remain Above 95% in 2024. Available online: https://www.ecns.cn/news/cns-wire/2024-12-16/detail-ihekzifh3684790.shtml?utm_source=chatgpt.com (accessed on 9 January 2025).
5. Liu, Z.; Liu, B.; Ding, X.; Wang, F. Research on Optimization of Energy Storage Regulation Model Considering Wind–Solar and Multi-Energy Complementary Intermittent Energy Interconnection. *Energy Rep.* **2022**, *8*, 490–501. [CrossRef]
6. Kemp, J.; Kemp, J. China's Rapid Renewables Rollout Hits Grid Limits. *Reuters*, 5 July 2024. Available online: <https://www.reuters.com/markets/commodities/chinas-rapid-renewables-rollout-hits-grid-limits-2024-07-04/> (accessed on 9 January 2025).
7. Mitali, J.; Dhinakaran, S.; Mohamad, A.A. Energy Storage Systems: A Review. *Energy Storage Sav.* **2022**, *1*, 166–216. [CrossRef]
8. Davison, J.; Arienti, S.; Cotone, P.; Mancuso, L. Co-Production of Hydrogen and Electricity with CO₂ Capture. *Int. J. Greenh. Gas Control* **2010**, *4*, 125–130. [CrossRef]
9. Hydrogen Storage. Available online: <https://www.energy.gov/eere/fuelcells/hydrogen-storage> (accessed on 7 October 2024).
10. Hashemi, L.; Glerum, W.; Farajzadeh, R.; Hajibeygi, H. Contact Angle Measurement for Hydrogen/Brine/Sandstone System Using Captive-Bubble Method Relevant for Underground Hydrogen Storage. *Adv. Water Resour.* **2021**, *154*, 103964. [CrossRef]
11. Tarkowski, R. Underground Hydrogen Storage: Characteristics and Prospects. *Renew. Sustain. Energy Rev.* **2019**, *105*, 86–94. [CrossRef]

12. Lemieux, A.; Sharp, K.; Shkarupin, A. Preliminary Assessment of Underground Hydrogen Storage Sites in Ontario, Canada. *Int. J. Hydrogen Energy* **2019**, *44*, 15193–15204. [CrossRef]
13. Gas Storage and Availability. Vattenfall. Available online: <https://group.vattenfall.com/what-we-do/market-transparency/gas-storage> (accessed on 8 October 2024).
14. Sambo, C.; Dudun, A.; Samuel, S.A.; Esenenjor, P.; Muhammed, N.S.; Haq, B. A Review on Worldwide Underground Hydrogen Storage Operating and Potential Fields. *Int. J. Hydrogen Energy* **2022**, *47*, 22840–22880. [CrossRef]
15. Caglayan, D.G.; Weber, N.; Heinrichs, H.U.; Linßen, J.; Robinius, M.; Kukla, P.A.; Stolten, D. Technical Potential of Salt Caverns for Hydrogen Storage in Europe. *Int. J. Hydrogen Energy* **2020**, *45*, 6793–6805. [CrossRef]
16. Valle-Falcones, L.M.; Grima-Olmedo, C.; Mazadiego-Martínez, L.F.; Hurtado-Bezos, A.; Eguilior-Díaz, S.; Rodríguez-Pons, R. Green Hydrogen Storage in an Underground Cavern: A Case Study in Salt Diapir of Spain. *Appl. Sci.* **2022**, *12*, 6081. [CrossRef]
17. Matos, C.R.; Carneiro, J.F.; Silva, P.P. Overview of Large-Scale Underground Energy Storage Technologies for Integration of Renewable Energies and Criteria for Reservoir Identification. *J. Energy Storage* **2019**, *21*, 241–258. [CrossRef]
18. Lemieux, A.; Shkarupin, A.; Sharp, K. Geologic Feasibility of Underground Hydrogen Storage in Canada. *Int. J. Hydrogen Energy* **2020**, *45*, 32243–32259. [CrossRef]
19. Li, L.; Yin, S.; Wang, Z. A Preliminary Assessment of Underground Space Resources for Hydrogen Storage in Salt Caverns in Lambton County, Southern Ontario, Canada. *Mining* **2024**, *4*, 530–545. [CrossRef]
20. Davoodi, S.; Al-Shargabi, M.; Wood, D.A.; Longe, P.O.; Mehrad, M.; Rukavishnikov, V.S. Underground Hydrogen Storage: A Review of Technological Developments, Challenges, and Opportunities. *Appl. Energy* **2025**, *381*, 125172. [CrossRef]
21. Oni, B.A.; Bade, S.O.; Sanni, S.E.; Orodu, O.D. Underground Hydrogen Storage in Salt Caverns: Recent Advances, Modeling Approaches, Barriers, and Future Outlook. *J. Energy Storage* **2025**, *107*, 114951. [CrossRef]
22. Cyran, K. Insight Into a Shape of Salt Storage Caverns. *Arch. Min. Sci.* **2020**, *65*, 363–398. [CrossRef]
23. Williams, J.D.O.; Williamson, J.P.; Parkes, D.; Evans, D.J.; Kirk, K.L.; Sunny, N.; Hough, E.; Vosper, H.; Akhurst, M.C. Does the United Kingdom Have Sufficient Geological Storage Capacity to Support a Hydrogen Economy? Estimating the Salt Cavern Storage Potential of Bedded Halite Formations. *J. Energy Storage* **2022**, *53*, 105109. [CrossRef]
24. Parkes, D.; Evans, D.J.; Williamson, P.; Williams, J.D.O. Estimating Available Salt Volume for Potential CAES Development: A Case Study Using the Northwich Halite of the Cheshire Basin. *J. Energy Storage* **2018**, *18*, 50–61. [CrossRef]
25. Rine, M.J.; McLaughlin, P.I.; Bancroft, A.M.; Harrison, W.B.; Kuglitsch, J.; Caruthers, A.H.; Ramezani, J.; Kaczmarek, S.E.; Emsbo, P. Linked Silurian Carbon Cycle Perturbations, Bursts of Pinnacle Reef Growth, Extreme Sea-Level Oscillations, and Evaporite Deposition (Michigan Basin, USA). *Palaeogeogr. Palaeoclimatol. Palaeoecol.* **2020**, *554*, 109806. [CrossRef]
26. Liu, W.; Dong, Y.; Zhang, Z.; Li, L.; Jiang, D.; Fan, J.; Chen, J.; Zhang, X.; Wan, J.; Li, Z. Optimization of Operating Pressure of Hydrogen Storage Salt Cavern in Bedded Salt Rock with Multi-Interlayers. *Int. J. Hydrogen Energy* **2024**, *58*, 974–986. [CrossRef]
27. Li, Z.; Fan, J.; Fourmeau, M.; Chen, J.; Jiang, D.; Nelias, D. Long-Term Deformation of Rock Salt Under Creep–Fatigue Stress Loading Paths: Modeling and Prediction. *Int. J. Rock Mech. Min. Sci.* **2024**, *181*, 105861. [CrossRef]
28. Nassan, T.H.; Kirch, M.; Amro, M. Underground Hydrogen Storage in Salt Caverns: Laboratory Experiments to Determine Integrity of Rock Salt and Wellbore through Effective Permeability Measurements. *Int. J. Hydrogen Energy* **2025**, *99*, 619–631. [CrossRef]
29. Zhang, Y.; Yang, L.; Huang, W. Study on Hydrogen Flow and Heat Transfer in Underground Salt Cavern Hydrogen Storage. *J. Phys. Conf. Ser.* **2023**, *2599*, 012017. [CrossRef]
30. Grgic, D.; Al Sahyouni, F.; Golfier, F.; Moumni, M.; Schoumacker, L. Evolution of Gas Permeability of Rock Salt Under Different Loading Conditions and Implications on the Underground Hydrogen Storage in Salt Caverns. *Rock Mech. Rock Eng.* **2022**, *55*, 691–714. [CrossRef]
31. Naderi, H.; Hekmatnejad, A.; Aftab, A.; Sarmadivaleh, M.; Pena, A. Integrating 1D and 3D Geomechanical Modeling to Ensure Safe Hydrogen Storage in Bedded Salt Caverns: A Comprehensive Case Study in Canning Salt, Western Australia. *Int. J. Hydrogen Energy* **2024**, *81*, 1073–1090. [CrossRef]
32. Deng, F.; Jiang, F.; Wan, J.; Ji, W.; Li, J. Analysis of the Deformation Characteristics of Surrounding Rock Due to Interlayers during Cyclic Injection-Production Period of Salt Cavern Hydrogen Storage. *Fuel* **2025**, *385*, 134115. [CrossRef]
33. Dias, W.; Roehl, D.; Mejia, C.; Sotomayor, P. Cavern Integrity for Underground Hydrogen Storage in the Brazilian Pre-Salt Fields. *Int. J. Hydrogen Energy* **2023**, *48*, 26853–26869. [CrossRef]
34. Carter, T. Bedded Salt in Ontario: Geology, Solution Mining and Cavern Storage. In Proceedings of the Ontario Petroleum Institute’s 48 Annual Conference: Ontario Oil, Gas and Storage Conference, Sarnia, ON, Canada, 10–12 November 2009.
35. Drucker-Prager Criterion—ProQuest. Available online: <https://www.proquest.com/docview/1114283355?accountid=14906&parentSessionId=009lmQYtpEmaQrytQSxrvu+eWyUhsFF82rIAZqnZ/Qw=&pq-origsite=primo&sourcetype=Scholarly%20Journals> (accessed on 4 November 2024).

36. Ozarslan, A. Large-Scale Hydrogen Energy Storage in Salt Caverns. *Int. J. Hydrogen Energy* **2012**, *37*, 14265–14277. [[CrossRef](#)]
37. Zhao, K.; Liu, Y.; Li, Y.; Ma, H.; Hou, W.; Yu, C.; Liu, H.; Feng, C.; Yang, C. Feasibility Analysis of Salt Cavern Gas Storage in Extremely Deep Formation: A Case Study in China. *J. Energy Storage* **2022**, *47*, 103649. [[CrossRef](#)]

Disclaimer/Publisher’s Note: The statements, opinions and data contained in all publications are solely those of the individual author(s) and contributor(s) and not of MDPI and/or the editor(s). MDPI and/or the editor(s) disclaim responsibility for any injury to people or property resulting from any ideas, methods, instructions or products referred to in the content.